



HEPH-Hassard-2

Detection of Improvised Explosive Devices using Neutron Activation and Gamma Spectroscopy

CID: 00936819

Supervisor: Dr John Hassard

Assessor: Dr Deep Chana

April 30, 2018

Word count: 9973

Contents

1	Introduction	2
2	Theory	2
2.1	How are Neutrons Generated?	2
2.2	Interactions of Neutrons with Matter	3
2.3	General Features of Gamma Spectra	4
2.3.1	Photo-peak	6
2.3.2	Compton Edge and Plateau	6
2.3.3	Compton Valley	6
2.3.4	Single and Double Escape Peaks	7
2.4	Scintillator Detectors	7
2.5	Semiconductor Detectors	8
2.6	Non-ideal Detector Response	10
2.7	Single and Multi-channel Pulse Height Analysers	11
2.8	Theory of Trichromatic Vision and Spectrally Selective Filters	11
3	Methodology	13
3.1	Geant4 Simulations	13
3.2	Modelling Detector Response Function	13
3.3	Baseline Correction using the Asymmetric Least Squares Method . .	17
3.4	Artificial Neural Network (ANN)	19
4	Analysis	22
4.1	Chromatic Detection Technique: Using Spectrum Filters	22
4.2	Bismuth Germanate (BGO) Detector	25
4.3	High Purity Germanium (HPGe) Detector	26
4.4	Predictive Capabilities of the BGO and HPGe Detectors	27
5	Conclusion	32
6	Acknowledgements	32
7	Appendix	38
7.1	Substances Simulated in Geant4	38
7.2	Modelling the Resolution of the HPGe Detector	38
7.3	Composition of Fictitious Materials	39
7.4	ANN Predictions Using BGO and HPGe Detectors	39
7.5	Candidate Materials for Spectrally Selective Filters	41

Abstract

The aim of this project was to investigate the feasibility of using neutron activation and gamma spectroscopy as a replacement for X-ray imaging for the detection of explosives. Two different methods have been evaluated for their ability to discriminate between materials with different elemental compositions: one uses spectrally selective filters and works in the same way to how the human eye discriminates between different colours of light; the other uses a machine learning approach to find the complex relationship mapping the photon counts as a function of energy in the gamma spectra to the percentage compositions of Hydrogen, Carbon, Nitrogen and Oxygen of the material. The first approach has been found to be unfeasible as no appropriate spectrum filter could be found for the 2-4MeV range. For the second approach, an artificial neural network (ANN) has been trained using gamma spectra obtained from particle simulations run in Geant4. Its predictive capabilities have been tested using Bismuth Germanate (BGO) and high-purity Germanium (HPGe) detectors. The false positive detection rates of the two detectors have been calculated as 60% and 20% respectively.

1 Introduction

With the number of terrorist-related deaths in non-conflict countries reaching a post-1985 high in 2014 [1], there is greater impetus amongst governments in both the US and Europe for improving their security infrastructure. The global security detection system market is forecast to reach \$5.3 billion in 2022, with much of the growth being driven by government spending on security systems due to the increased concern of the use of improvised explosive devices (IEDs) [2]. Hence, the ability to provide an effective explosive detection system for the protection of critical targets is of increased importance for national governments [3]. At the moment, the inspection of luggage and freight at airports and shipping ports relies predominantly on the attenuation of X-rays through matter: these range from simple transmission imaging to multi-energy and 3-dimensional computed tomographic imaging [4] (see Fig. 1). With these it is possible to gain information about the density profile and tomography of an inspected sample [4], which can be used to discriminate between contraband and benign objects inside it. Unfortunately, none of the detection methods based on the use of X-rays have been shown to provide enough discrimination to be able to differentiate between a plastic explosive and a bag of flour of the same shape [4]. Furthermore, the inspected sample can be shielded from X-rays by high-Z material; this further degrades the ability of the system to detect explosives and contributes to it having high false positive rates [4]. Hence, there is a gap in our current explosive detection capabilities which would need to be filled to reduce the threat posed by the use of explosives to both people and critical infrastructure. This report focuses on the possible application of neutron activation and gamma spectroscopy as a replacement to X-ray imaging for the detection of explosives.

2 Theory

2.1 How are Neutrons Generated?

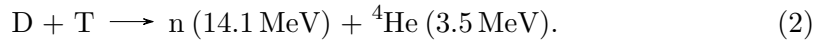
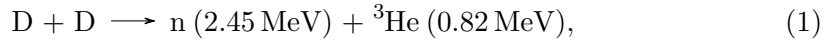
The source of neutrons in neutron activation analysis comes from four basic interaction mechanisms: the radioactive decay of a neutron emitter; the pairing of an alpha particle emitter and an alpha particle absorber to produce neutrons via the (α, n) interaction; the photo-excitation of nuclei with highly-energetic gamma rays to

Figure 1: A CT X-ray image of a piece of luggage [5].



stimulate the emission of neutrons via the (γ, n) interaction; and the use of compact neutron generators [6].

The type of source chosen depends on which neutron interactions are to be used to assay a sample. For neutron activation analysis and gamma ray spectroscopy, inelastic scattering of neutrons ($n, n' \gamma$) can be used to determine the composition of the sample [7]. Incoming neutrons with a kinetic energy below a certain threshold will not interact via this interaction [8]; hence, it is important that the source is chosen such that the neutrons have an energy above the thresholds of all the elements that comprise the sample. This can be achieved using neutron generators: these are devices which rely on either the Deuterium-Deuterium (D-D) or Deuterium-Tritium (D-T) fusion reactions to produce a mono-energetic source of 2.45MeV and 14.1MeV neutrons respectively [9]:



However, as the yield of the D-T reaction is approximately two orders of magnitude greater, it is common to use this reaction instead of the D-D reaction in commercial neutron generators [10].

2.2 Interactions of Neutrons with Matter

When neutrons pass through matter they can interact with the nuclei therein via a number of different interactions, which can be categorised according to whether the neutron was scattered or absorbed. When a neutron is scattered its direction and speed changes as some of its energy is imparted to the nucleus. In order to conserve momentum the nucleus will have a recoil velocity; furthermore, in some interactions the nucleus is left in an excited state and therefore emits a photon when it relaxes to a lower energy state [11]. When a neutron is absorbed the resulting nucleus can emit a variety of different particles which could be either charged or neutral [11]. Moreover, in some highly-energetic interactions the neutron interaction can lead to the fission of the nucleus [12].

The neutron scattering interactions can be split into those that involve elastic and inelastic scattering. The former involves the conservation of the combined kinetic energy of the neutron and nucleus, whereas in the latter the kinetic energy of this system decreases because some of the energy is used to put the nucleus in an excited state [11]. It can be shown that the kinetic energy of a neutron, E_f , that was elastically scattered by a stationary nucleus (n, n') is given by the following expression [8]:

$$E_f = \frac{1}{(1+A)^2} E_i \left(\cos^2 \theta + A^2 - \sin^2 \theta + 2 \cos \theta (A^2 - \sin^2 \theta)^{\frac{1}{2}} \right), \quad (3)$$

where E_i is the initial kinetic energy of the neutron; A is the ratio between the mass of the nucleus, M , and the neutron mass, m_n , i.e., $A = \frac{M}{m_n}$; and θ is the neutron scattering angle.

For inelastic scattering ($n, n' \gamma$), the nucleus undergoes internal rearrangement and therefore the final kinetic energy of the scattered neutron depends on the internal structure of the nucleus [13]. If we assume that the binding energy of the nucleus is E^* and that the nucleus was initially stationary, then it can be shown that there is a minimum threshold for the initial kinetic energy of the neutron, E_t , [8]:

$$E_t = E^* \left(\frac{M + \frac{E^*}{c^2}}{M - m + \frac{E^*}{c^2}} \right); \quad (4)$$

hence, the threshold energy for inelastic scattering is always more than the binding energy of the nucleus; this is because some of the energy is also transferred to the recoiling nucleus. As the binding energy of the nucleus is usually in the MeV range, it is necessary to use a source that produces highly energetic neutrons- this can be achieved using the D-T neutron generators (see section 2.1).

When a neutron is absorbed by a scattering nucleus, the latter can undergo a rearrangement of its nuclear structure and subsequently relax to a stable configuration via the emission of a photon- this is called radiative capture (n, γ) [11]. The other possibilities are that the nucleus releases one or more neutrons, with the former giving the same interaction mechanism as elastic scattering (n, n'), or that it releases charged particles- the most common being protons, alpha particles and deuterons [11].

2.3 General Features of Gamma Spectra

The main process by which photons are detected, whichever type of detector used (e.g., scintillator, semiconductor or gas-filled radiation detectors), is by the ionisation of atomic electrons in the detector material [14]. These can be ionised via a number of different electromagnetic interactions and in each one the photon gives up either all or a fraction of its original energy. The two main types of interactions that occur are the photoelectric effect and Compton scattering [14]- where in the former the photon imparts all of its energy to the electron and in the latter it only imparts some of its energy. In the photoelectric effect, the kinetic energy of the liberated electron, ϵ_k , is determined by how strongly it was originally bound to the nucleus [14]:

$$\epsilon_k = h\nu - \epsilon_b, \quad (5)$$

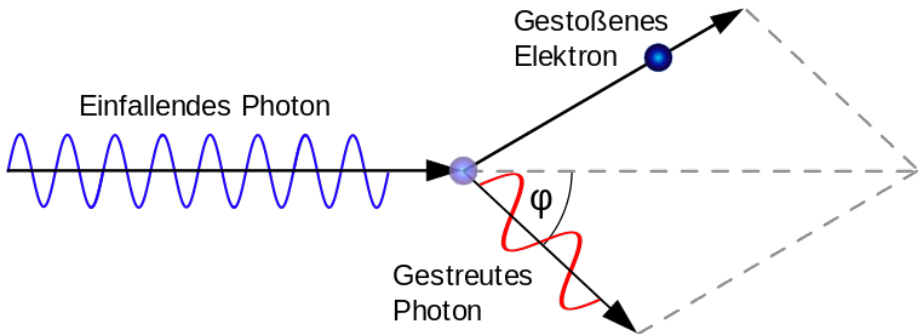
where $h\nu$ is the photon energy and ϵ_b is the binding energy of the atomic electron. Therefore, if the photon energy is much greater than the atomic binding energy, the kinetic energy of the liberated photon is approximately equal to the energy of the incident photon, $\epsilon_k \approx h\nu$.

In contrast, if the atomic electron interacts with a photon via Compton scattering, then- assuming that the energy imparted by the photon to the electron is high enough to consider the electron to have been unbound- the kinetic energy of the liberated electron is given by [15]:

$$\epsilon_k = h\nu \left(1 - \frac{1}{1 + \frac{h\nu(1-\cos\phi)}{m_e c^2}} \right), \quad (6)$$

where $m_e c^2$ is the rest mass energy of the electron and ϕ is the scattering angle (see Fig. 2). An electron which is liberated by either the photoelectric effect or Compton scattering then goes on to ionise further atomic electrons via collisions until its energy is entirely depleted [14]. The total number of these charge carriers created by each detection event is linearly proportional to the total energy that was initially deposited by the photon. Thus, there is also a linear relationship between the electrical pulse caused by these charges and the energy deposited by the photon [14]. This is the principle method for discriminating between the energy of photons in any type of detector.

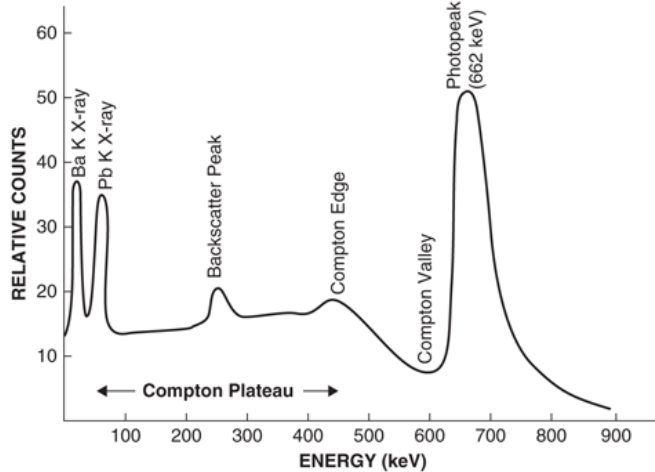
Figure 2: Schematic diagram of the Compton scattering interaction. The incident photon (blue) is scattered by an angle ϕ (red) and the electron recoils to conserve energy and momentum [17].



Another type of interaction that could occur within the detector is electron-positron pair production. This can only take place when a photon is immersed within a very intense electric field, such as in the vicinity of a nucleus [16]. Furthermore, as the products of this interaction are an electron and a positron, only photons with an energy more than their combined rest mass energy, $2m_e c^2$, can interact via pair production [14].

Fig. 3 illustrates the features that are common to all gamma spectra. Instead of obtaining a Dirac delta peak at the photon energy, the spectrum is a continuum with peaks relating to the types of interactions that occur when a photon passed through a detector medium. The physical processes that cause these features are explained in the sections below.

Figure 3: The typical spectrum due to the emission of 662KeV photons from ^{137}Cs [18].



2.3.1 Photo-peak

This corresponds to incident photons that have each imparted all of their energy to an atomic electron via the photoelectric effect [14]; this is the reason why the peak is centred at the same energy as the incident photons. It is broadened due to statistical fluctuations in the number of charge carriers that are formed as a result of the collisions of liberated electrons [14]. Furthermore, if the detector is connected to a photomultiplier tube (PMT) there will be another contribution to the width which is due to the statistical fluctuation in the number of secondary electrons that are set free at each dynode.

2.3.2 Compton Edge and Plateau

In Compton scattering the amount of energy that the photon imparts to the electron is a continuum corresponding to the range of possible scattering angles, $0 \leq \phi \leq \pi$. From equation 6, it can be shown that the minimum energy imparted to the electron is zero and occurs when $\phi = 0$, which corresponds to there being no interaction taking place between the photon and electron. Conversely, when $\phi = \pi$, which corresponds to the maximum change in momentum of the incident photon, the energy imparted to the liberated electron is a maximum and its value, ϵ_c , is given by:

$$\epsilon_c = h\nu \left(1 - \frac{1}{1 + \frac{2h\nu}{m_e c^2}} \right). \quad (7)$$

This energy corresponds to the Compton edge and is a clearly visible feature on most gamma-ray spectra. Another feature of gamma spectra is the Compton plateau: this is the continuum of the energy spectra due to singly scattered electrons with $0 \leq \phi < \pi$.

2.3.3 Compton Valley

This feature is due to electrons that have undergone multiple Compton scattering interactions, and in each scattering event the kinetic energy of the electron has been

increased [19]. These electrons also contribute to the Compton plateau but as the cross section for multiple Compton scattering is much less than for single Compton scattering [20] they make a negligible contribution to this region.

2.3.4 Single and Double Escape Peaks

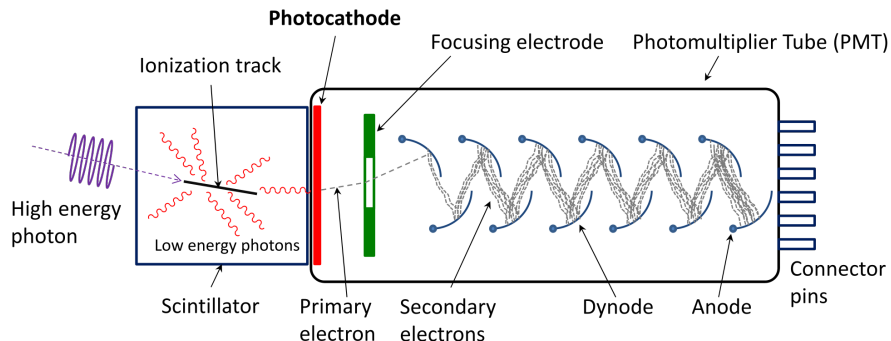
When an incident photon interacts via pair production, an electron and positron, each with an energy equal to their rest mass energy, $m_e c^2$, are produced. The latter is incredibly unstable and quickly annihilates another electron within the detector. This results in the production of two photons that each have an energy of $m_e c^2$ [14]. Due to the finite geometry of the detector it is possible that one or both of the photons escapes and therefore does not deposit its energy within the detector. If only one photon escapes, then the total energy deposited in the detector is equal to $h\nu - m_e c^2$, which corresponds to the single escape peak. On the other hand, if both electrons escape, then only $h\nu - 2m_e c^2$ is deposited, which results in the double escape peak [21].

2.4 Scintillator Detectors

One of the main types of gamma-ray detector is one that is made from scintillating material. These materials, which can be organic or inorganic, are ones in which its atoms decay and primarily emit visible light photons- this occurs after they are photo-excited by the absorption of more highly-energetic photons.

Fig. 4 demonstrates the basic operating principles of a scintillator detector. A highly-energetic photon that is incident on the scintillating material deposits energy along its path, which is released in the form of visible light when the photo-excited atoms or molecules within the scintillator decay back to a stable state. These photons are then converted to photo-electrons at a photo-cathode, which is often connected to a PMT in order to amplify the electronic signal. As the relation between the intensity of visible light emitted and the energy deposited per unit path length of the gamma-ray photon is known, the energy of the incident photon can be determined by the amplitude of the resultant electric pulse. In an inorganic scintillator the two are approximately linearly proportional, whereas, in an organic scintillator their relationship is governed empirically by Birk's Law [22]. The reason for the non-linearity of the inorganic-based scintillators is because of the effects of quenching: a high density of excited molecules along the path of the incident gamma-ray photon saturate the light output and de-excite without emitting photons [23].

Figure 4: A schematic diagram of the detection of a highly-energetic photon by a scintillator detector [24].

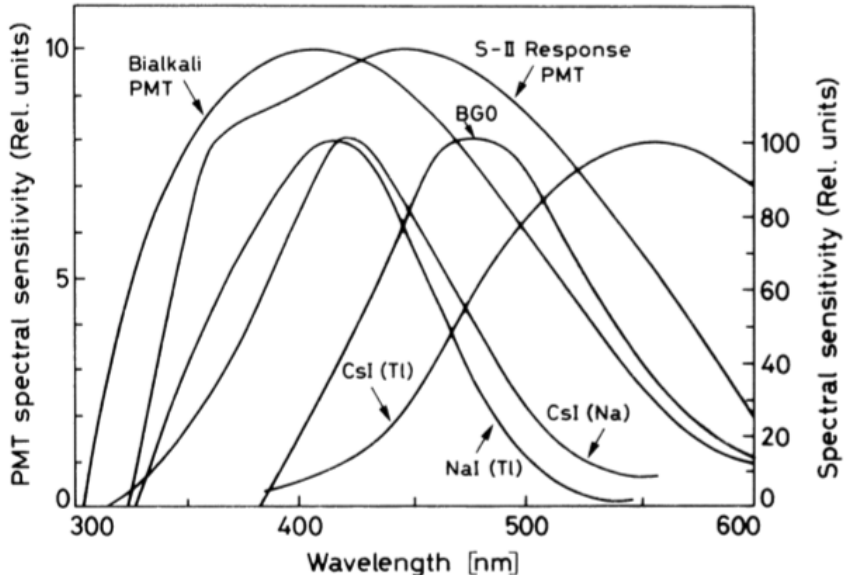


An ideal scintillating material for detecting gamma-ray photons is one that has the following characteristics [23]:

- high conversion of gamma-ray radiation to visible light;
- its emission spectrum coincides with the spectral sensitivity of the photocathode;
- and the material is transparent to its own fluorescent radiation to prevent re-absorption.

The emission spectra of an inorganic scintillator called Bismuth Germanate (BGO) is shown in Fig. 5. The photo-fluorescence of this material is governed by its band structure as the emission of photons is caused by the recombination of electrons in the conduction band and holes in the valence band [23]. Its emission curve peaks at a wavelength of 480nm [23], which fortunately overlaps with the spectral sensitivities of a lot of PMTs making it effective for photo-detection.

Figure 5: A plot of the emission spectra of some commonly used inorganic scintillators (right axis) and the spectral sensitivity of two photo-multiplier tubes (left axis) [28].

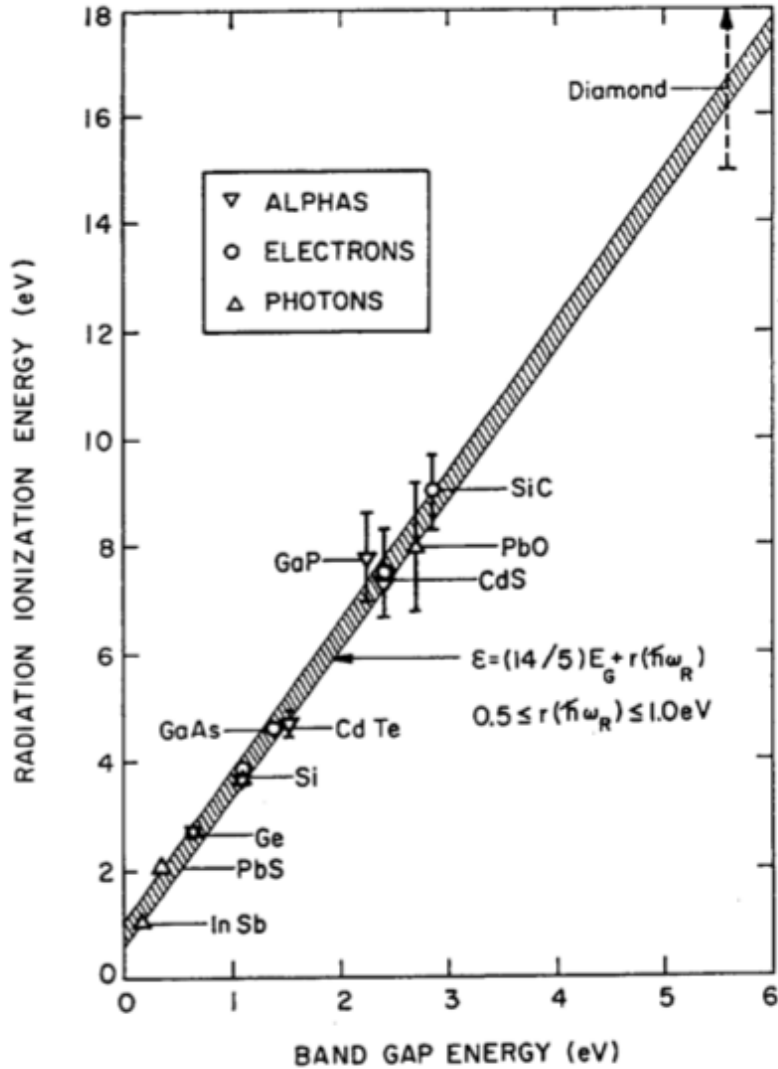


2.5 Semiconductor Detectors

In semiconductor detectors, ionising radiation is measured by the number of electron-hole pairs created when a photon deposits its energy within the depletion region [25]. An external electric field is applied across it, which accelerates the electrons and holes in opposite directions, and the charge collected at the electrodes produces an electronic pulse which can be measured [26]. As the average amount of energy required to create an electron-hole pair is known and is almost independent of the energy of the incident photon [27]- it is, instead, linearly proportional to the band gap of the semiconductor (see Fig. 6)- a measurement of the number of electron-hole pairs can be used to determine the energy of the original photon. If the average energy needed to create an electron-hole pair is given by ϵ_{e-h} and the energy of the incident photon is $\hbar\nu$, then the average number of electron-hole pairs created when a photon of this energy interacts within the detector, \bar{n} , is given by [29]:

$$\bar{n} = \frac{h\nu}{\epsilon_{e-h}}. \quad (8)$$

Figure 6: A plot showing the linear relationship between the band gap energy (eV) of a semiconductor material and mean energy used for ionisation [32].



If the energy imparted by each interaction of the incident photons was only due to pair production then the number of electron-hole pairs created would be accurately represented by Poisson statistics meaning that the statistical fluctuation in n would be given by [30]:

$$\sigma_n = \sqrt{\bar{n}} = \sqrt{\frac{h\nu}{\epsilon_{e-h}}}. \quad (9)$$

However, it is usual for some of the energy imparted by the photon to be used for non-ionising excitations; the most common examples of this type of excitation are molecular vibrations and the creation of phonons in the crystal lattice structure [31]. This reduces the number of electron-hole pairs created by the passage of a single photon through the detector medium. Moreover, the observation of an electron-hole

pair at the electrodes of the semiconductor is no longer a completely independent event as it now depends on the number of non-ionising excitations that occur. This means that Poisson statistics do not accurately predict the statistical fluctuations in the number of charge carriers that are collected at the two electrodes. Instead, it can be shown that the following expression holds for the statistical fluctuation in the number of ionisations, σ_{ion} , [30]:

$$\sigma_{ion} = \sqrt{\frac{E}{\epsilon_{e-h}}} \cdot \sqrt{\frac{E_{phon}}{E_{ion}} \left(\frac{\epsilon_{e-h}}{E_{ion}} - 1 \right)} = \sqrt{\frac{F \cdot E}{\epsilon_{e-h}}}, \quad (10)$$

where the expression under the second square root is called the Fano Factor, F . It can further be demonstrated, if one assumes that there is a sufficiently high photon flux incident for the central limit theorem to apply to the number of charge carriers created, that the energy resolution of a semiconductor detector is [30]:

$$R = \frac{FWHM}{\langle N_q \rangle} = 2 \cdot \sqrt{2 \ln 2} \cdot \sqrt{\frac{F \cdot \epsilon_{e-h}}{E}}, \quad (11)$$

where FWHM is the full-width-at-half-maximum of the electrical pulse and $\langle N_q \rangle$ is the mean number of charged particles created due to the detection of a photon with energy E . It can be deducted, using equations 10 and 11 and Fig. 6, that a semiconductor with a smaller band gap is better at discriminating the energies of photons and, therefore, the photopeaks that appear in their gamma spectra are much more highly resolved. However, semiconductors with smaller band gaps have a problem, which can be seen by looking at the expression for the number of electrons in the conduction band, n_e , when the semiconductor is in thermodynamic equilibrium [33]:

$$n_e = 2 \left(\frac{K_B T m_e^*}{2\pi \hbar^2} \right)^{\frac{3}{2}} e^{-(\frac{\epsilon_c - \mu}{K_B T})}, \quad (12)$$

where m_e^* is the effective mass of the electrons; $K_B T$ is the thermal energy; ϵ_c is the minimum energy of the conduction band; and μ is the Fermi level of the semiconductor. Hence, when the band gap of the semiconductor is small the number of electrons ionised to the conduction band is very sensitive to the temperature of the detector device. Therefore, for small band gap semiconductors such as Germanium, which has a band gap of 0.66eV at 300K [34], the detector needs to be kept at very low temperatures. For instance, High Purity Germanium (HPGe) detectors are optimised at cyrogenic temperatures ($\leq 120K$) [35], which is often achieved using a liquid nitrogen coolant. This requirement limits their applicability because of the hazardous nature of liquid nitrogen and the increased maintenance costs associated with operating them [35].

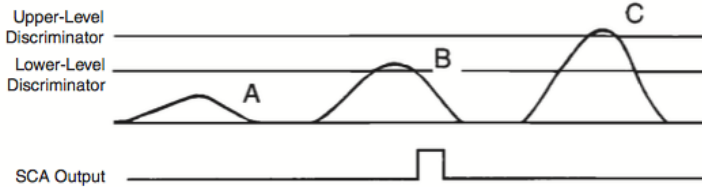
2.6 Non-ideal Detector Response

Beyond those already broached, there are some other factors which can contribute to a detector having a non-ideal response function. Some of the most important ones are: secondary electron escape, Bremsstrahlung escape, characteristic X-ray escape, Auger electron escape, radiation from surrounding material and also the detection of more than one gamma-ray photon coincidentally. The extent to which each of these factors contributes to the non-ideal response of a detector depends on both the detector's geometry and with what material it is made from [36, 37, 38, 39, 40].

2.7 Single and Multi-channel Pulse Height Analysers

When a photon is incident on a detector and interacts via one of the interaction mechanisms discussed in section 2.3, a weak electrical signal is detected which has an amplitude that is proportional to the energy of the incident photon. The spectrum of the incident photon flux can be determined by using either a single or multi-channel pulse height analyser. These work by producing an output logic pulse when the peak amplitude of the input signal is between two pre-set threshold values [41] (see Fig. 7). Hence, in conjunction with a counter this can be used to count the total number of photons incident on a detector within a set energy interval. The difference between the single and multi-channel pulse height analysers is that the former only detects photons within one set energy interval, whereas the latter splits the spectrum into multiple energy bins and detects photons separately according to their energies- this can be used to produce a histogram of the photon counts. One source of uncertainty in such a device is when there are two input signals which cannot be time resolved, which happens when more than one photon is incident on the detector and the time between their detection is small enough so that their signals are superimposed on top of each other. This results in so-called coincident photon peaks with an energy that is double the photopeak as discussed in section 2.6.

Figure 7: The single channel pulse height analyser acts to produce an output logic signal only if the amplitude of the input signal is between the two discriminatory levels [42].

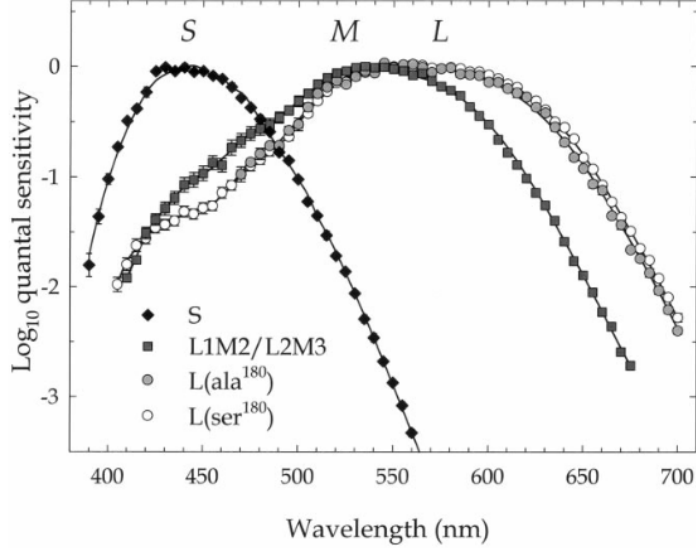


2.8 Theory of Trichromatic Vision and Spectrally Selective Filters

The human eye can discern between millions of different colours using just three photo-receptor cells. These are called the S, M and L cone cells and their spectral response curves peak at the short, medium and long wavelengths of the visible light part of the electromagnetic spectrum respectively (see Fig. 8). They are excited to a varying degree when light of a particular wavelength is incident on them. The relative intensity of light that is measured by each of these three photo-sensitive detectors is sufficient to discriminate between all of the colours to which the human eye is sensitive [60].

It is hypothesised that the use of spectrally selective filters could be similarly used to discriminate between samples of material with different elemental compositions- this would be done using the gamma spectra obtained from neutron activation. In order for this method to work for the detection of explosives, there will need to exist several photo-detectors whose response functions peak at different photon energies covering the range of characteristic gamma-ray emissions of Hydrogen, Carbon, Nitrogen and Oxygen. However, as the photo-electric absorption cross section, which is the interaction responsible for producing the photo-peaks in the gamma spectra (see section 2.5.1), is fairly constant across the range of relevant photon energies [44], it would be necessary to place filters in front of the detectors so as to change the

Figure 8: The spectral response curves of the S, M and L cone cells of the human eye [45].



the energy dependence of the photon flux that is incident on the detectors. An ideal spectrum filter would be one that has a non-linear transmission curve with a maximum close to one of the characteristic gamma-ray emissions of the four elements. This increases the filter's selectivity and means that the gamma-ray detectors detect a greater number of photons within a narrow range of photon energies, which was hoped to be sufficient for discriminating between samples of different elemental compositions.

The physics of spectrum filters can be understood using the expression for the total gamma-ray transmission ratio, T_γ . This can be written as the product of the gamma-ray transmission ratios of each of the possible interaction mechanics discussed in section 2.5 [14]- as well as the photo-nuclear effect, which peaks at higher energies than both the photoelectric effect and Compton scattering [46]:

$$T_\gamma = \prod_i T_{\gamma_i} = e^{-n\sigma d}, \quad (13)$$

$$T_{\gamma_i} = e^{-n\sigma_i d},$$

$$\sigma = \sum_i \sigma_i,$$

where n is the particle number density; σ is the total gamma-ray absorption cross section, which can be decomposed into a linear sum of its partial absorption cross sections, σ_i ; and d is the thickness of the filter. A measure of the ability of a spectrum filter to discriminate between two photons of different energies, E_1 and E_2 , is the ratio between their transmissions through the filter, N :

$$N = \frac{T_\gamma(E_2)}{T_\gamma(E_1)} = e^{n(\sigma(E_1)-\sigma(E_2))d}. \quad (14)$$

3 Methodology

3.1 Geant4 Simulations

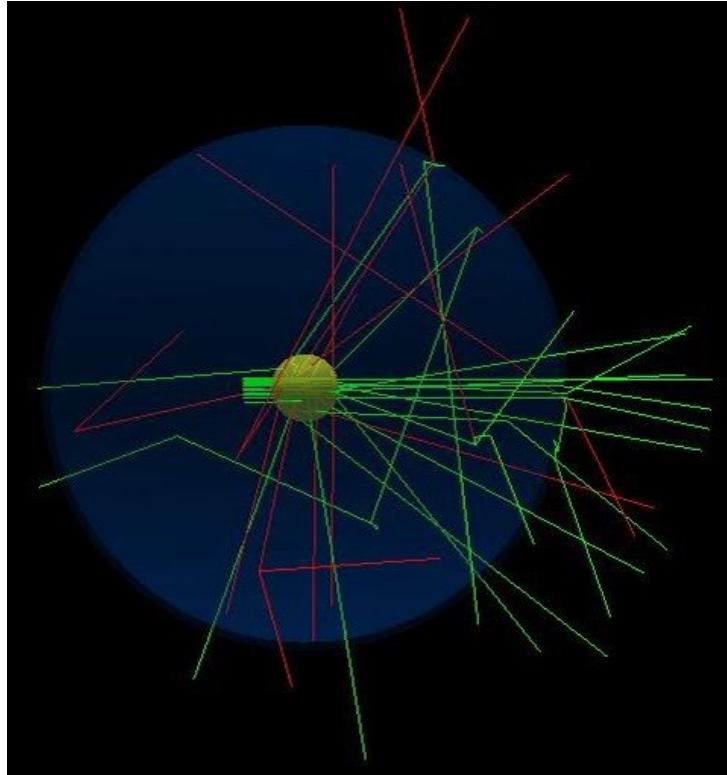
Simulations for assaying the samples with neutrons and the subsequent detection of the secondary particles emitted when the neutrons interact with the nuclei within the sample were done in Geant4. This is a toolkit developed by CERN for simulating the passage of particles through matter which relies on the application of Monte Carlo methods for the probabilistic nature of particle interactions [47]. Geant4 handles the modelling of the geometry of the detection environment, tracking of each particle within the so-called global volume- if a particle goes outside this volume then the simulation of the particle is stopped- and their detection by particle detectors. The geometry of the detection environment used in this study is shown in Fig. 9. It includes the sample that is to be assayed, which is modelled as a solid sphere with a radius of 10cm in the centre of the detection environment, and the gamma-ray detector, which is modelled as a spherical shell with a uniform thickness of 2.5cm and with its internal surface being an equidistant 75cm from the centre of the sample.

The composition of both the sample and the particle detector could be set for each simulation, and then Geant4 would use its internal database of particle cross sections to set the parameters of the particle simulations. For each Geant4 simulation, the composition of the particle detectors were either those for BGO [48, 49] or HPGe [50]. When BGO was used as the particle detector, a thin conversion layer with a thickness of $100\mu\text{m}$ was used to increase the conversion of photons to electrons in the detector and thus increase the detector efficiency. The composition of the samples was also altered by changing the ratio of the number of atoms of Hydrogen, Carbon, Nitrogen and Oxygen within it. Altering the composition led to a change in the height of the characteristic gamma-ray peaks in the gamma spectra, which could then be used as a fingerprint for the composition of the sample. The simulations were initialised with a beam of either 50 or 100 million neutrons with an energy of 14MeV, which were fired towards the sample and used to assay it. The former was used for simulations with the HPGe detector and the latter used with the BGO detector. The density of the samples was kept at a constant 1.20gcm^{-3} , which was reasonable because most explosives containing a combination of just Hydrogen, Carbon, Nitrogen and Oxygen have a density that is within an order of magnitude of this value [51].

3.2 Modelling Detector Response Function

The gamma spectra obtained by the Geant4 simulations were unrealistic as they did not take into account the non-ideal response of the gamma-ray detectors. Some of the main contributions to the non-ideal response of detectors are broached in sections 2.3.1 through 2.3.4 and 2.6. Some of these features are clearly visible on the gamma spectra obtained experimentally using the BGO and HPGe detectors as shown in Fig. 10. If a comparison is made between these two spectra, i.e., Fig. 10a and Fig. 10b, then the main differences between their features is that the FWHM of the photopeak in the spectrum obtained using the HPGe detector is much smaller than that obtained using the BGO detector; furthermore, the Compton edge is much more prominent in the latter than in the former. The reason for this is that the ratio between the cross sections for the gamma-ray photons to interact via the photoelectric effect and the Compton scattering interaction is much greater in the BGO detector than in the HPGe detector (see Fig. 11). This means that the

Figure 9: A schematic diagram of the geometry of the detection environment. The sample is the yellow solid sphere; the blue spherical shell is the outline of the detector; and the green and red lines represent the particle tracks of neutrons and secondary particles respectively.

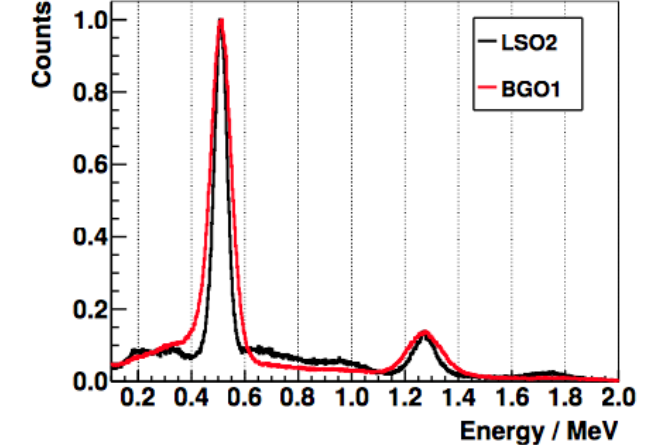


photons interacting within the BGO detector are much less likely to interact via the Compton scattering interaction and thus contribute to any of the Compton features in the gamma spectrum.

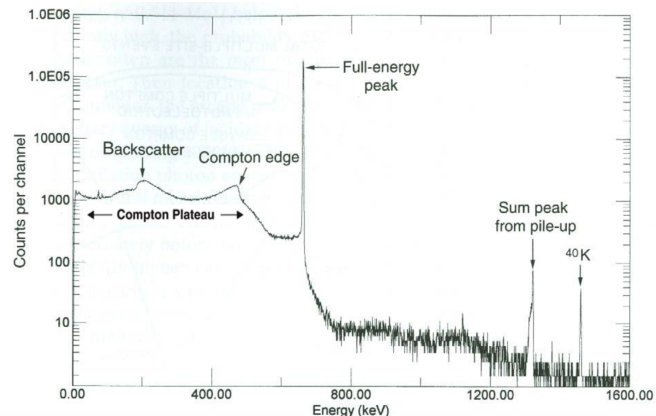
To quantify this further, the relative size of the photopeak to the Compton edge needs to be determined. This can be done semi-empirically by using the Klein-Nishina formula, which gives the differential cross section for photons scattered by a free electron, to find the fraction of scattered photons with an energy within 1KeV (chosen because it is within an order of magnitude of the bin widths used in our gamma spectra- see sections 4.2 and 4.3) of the Compton edge as a function of the incident photon energy, and then multiplying this by the “total” Compton scattering cross section, which is integrated over all scattering angles and has been determined experimentally [44]. This is plotted for both BGO and HPGe in Fig. 11a and 11b respectively. For both detectors the cross section for the photoelectric effect is greater than that for the “partial” Compton scattering interaction. This equates to the photopeak caused by a photon interacting in either detector being larger than the associated Compton edge. However, because these cross sections are of the same order of magnitude in the HPGe detector, the Compton edge is a much more prominent in its gamma spectra. At an incident photon energy of 4MeV, the photoelectric cross section is approximately 10^2 times greater than the “partial” cross section in the BGO detector but only double in the HPGe detector. Hence, we can safely neglect the Compton edge when modelling the response of the BGO detector and simply model the photopeak as a Gaussian curve. This assumption was also made when modelling the response of the HPGe detector but the gamma spectra obtained are thus less realistic.

Thus, the gamma spectra obtained from the Geant4 simulations using both the BGO and HPGe detectors were Gaussian smeared. The former with a constant resolution of 10% [52] and the latter using a varying resolution determined from regression analysis of experimental data [53] (see Appendix 7.2). The resolution of the HPGe detector is approximately a factor of 10^3 times smaller than for BGO.

Figure 10: Gamma spectra obtained experimentally using the BGO detector (a) and the HPGe detector (b) [54, 55] (the counts of the former are normalised to unity). The Compton edge is clearly more visible in the former than the latter.

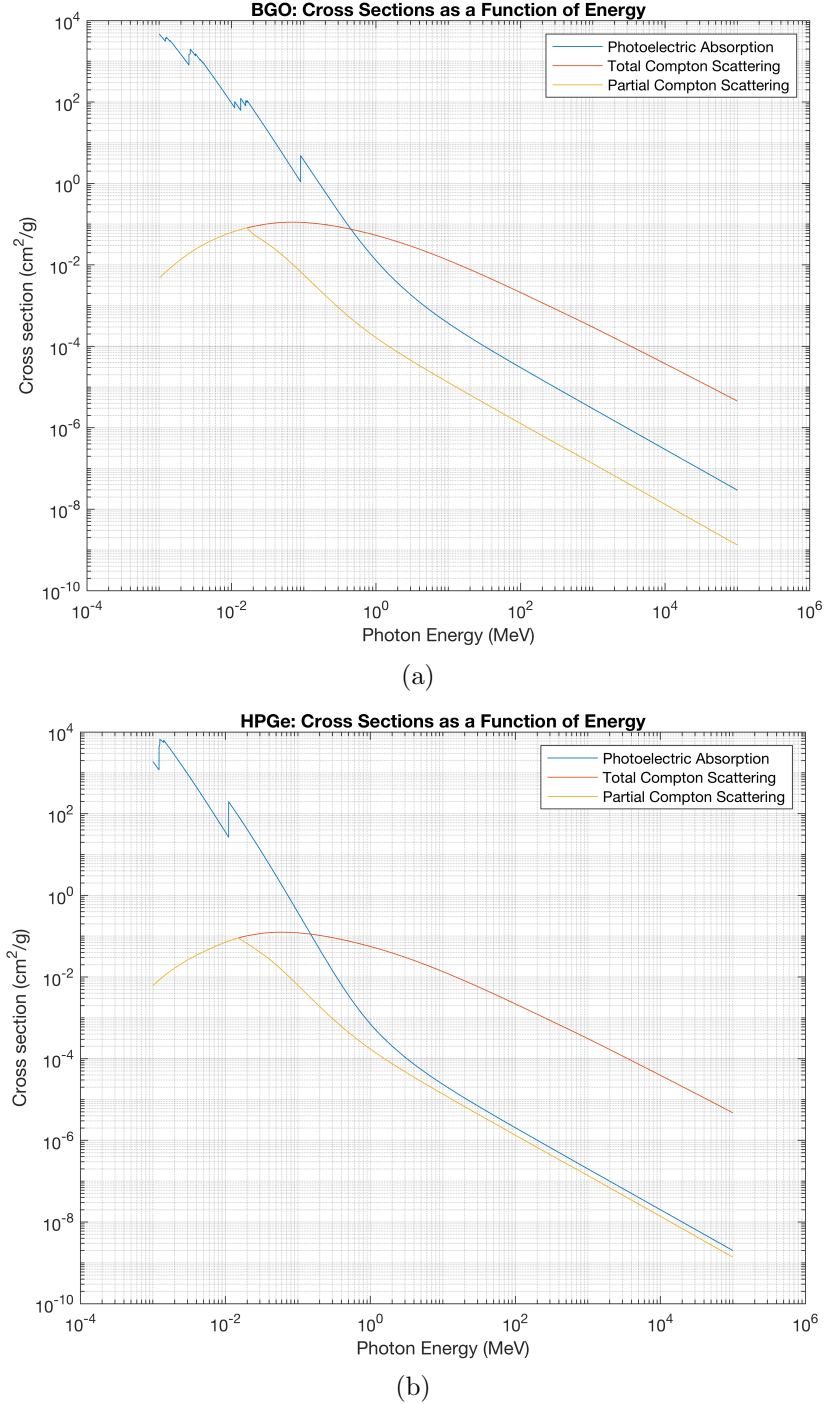


(a)



(b)

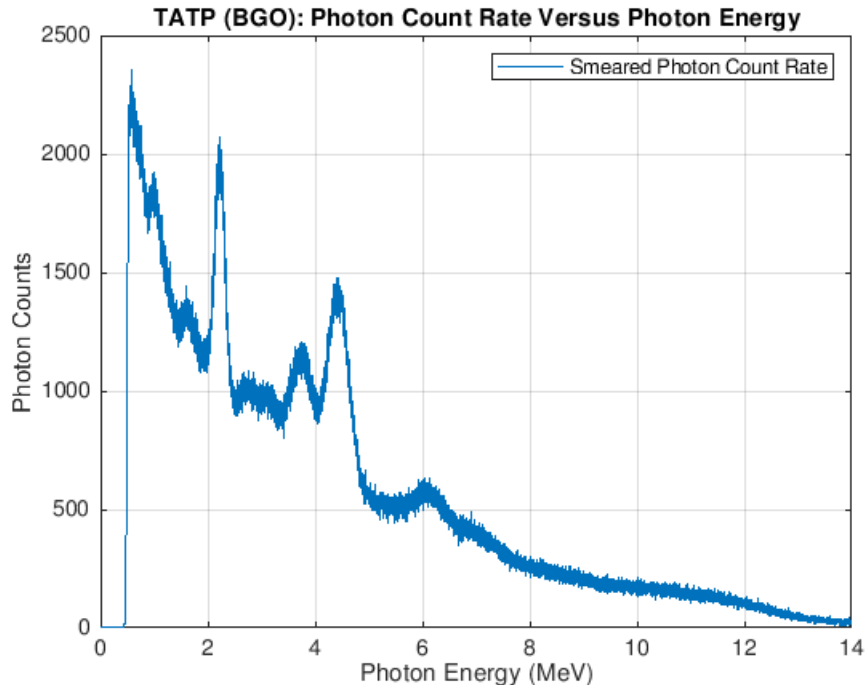
Figure 11: Log-log plot of the photoelectric and Compton scattering cross sections against incident photon energy for BGO (a) and HPGe (b). The cross sections for the photoelectric and total Compton scattering interactions have been extracted from the NIST database [44]. The partial Compton scattering cross sections, defined as the cross section for the outgoing photon to be within 1KeV of the Compton edge, has been calculated theoretically using the Klein-Nishina formula. When the Compton edge is below 1KeV the total and “partial” Compton scattering cross sections become equal because all scattered photons have an energy of within 1KeV of the Compton edge.



3.3 Baseline Correction using the Asymmetric Least Squares Method

The application of Gaussian smearing to the gamma spectra that were obtained from the simulations resulted in a “background”; this had an asymmetric peak that occurred at photon energies of approximately 0.5-0.6MeV and that decreased much more quickly towards lower energies than towards higher ones. This can be seen clearly in Fig. 12, which depicts the gamma spectrum of TATP with Gaussian smearing to model the response function of the BGO detector. One of the effects of Gaussian smearing has been to increase the relative height of the lower energy peaks compared to those at higher energies; hence, without isolating this effect, any detection-based system that relies on using the relative heights of the characteristic gamma-ray peaks for calculating the elemental composition of a sample would likely do the following: it would overestimate the percentage composition that is due to an element with characteristic gamma-ray peaks at lower energies compared to those with peaks at higher energies. For instance, the dominant peaks for Carbon and Nitrogen occur at 4.4MeV and 2.3MeV respectively; hence, the smearing of these peaks would result in the relative height of the Carbon peak appearing to be smaller in comparison to the Nitrogen peak than it would be for an ideal detector response. This would result in inaccurate predictions of the percentage compositions of these two elements. The only way to eliminate this distortion in the gamma-ray spectra is to calculate the “background” and then to subtract it from the total photon counts to give an estimate of the actual photon counts at each energy bin.

Figure 12: The gamma spectrum of TATP with Gaussian smearing to model the response of the BGO detector.



The baseline of the gamma spectra can be determined using a number of different algorithms, but the one that is most effectively applied to gamma spectra is the asymmetric least squares (ALS) method. This is the case because in gamma spectra the deviations from the baseline only occur on one side, i.e., there are no physically meaningful troughs in the spectra; this is well-treated within the ASL method since

the values occurring above the baseline are weighted less than those occurring below it. The asymmetry in the weightings is parameterised by the value p whereby the weighting of the values above the baseline estimate are assigned this value and those below it are given the weighting $1 - p$. Overall, the ASL method aims to determine the baseline by minimising the following function [56]:

$$S = \sum_i w_i(y_i - z_i)^2 + \lambda \sum_i (\Delta^2 z_i)^2, \quad (15)$$

$$\Delta^2 z_i = z_i - 2z_{i-1} + z_{i-2}, \quad (16)$$

where w_i is the weighting of the i^{th} value, y_i is the original signal strength and z_i is the baseline estimate. The first term on the right hand side of equation 15 measures how well the baseline fits the data, whereas the second term is a penalty on its non-smoothness. Hence, by minimising these two terms in conjunction, one can obtain a baseline that is both an accurate fit with the data and smooth; furthermore, the estimate of the baseline can be optimised by adjusting the two variable parameters: p for the asymmetry of the weightings and λ for the smoothness of the fit.

Implementation of the ASL method was done in Matlab using an iterative code [56]. This works by performing the following steps:

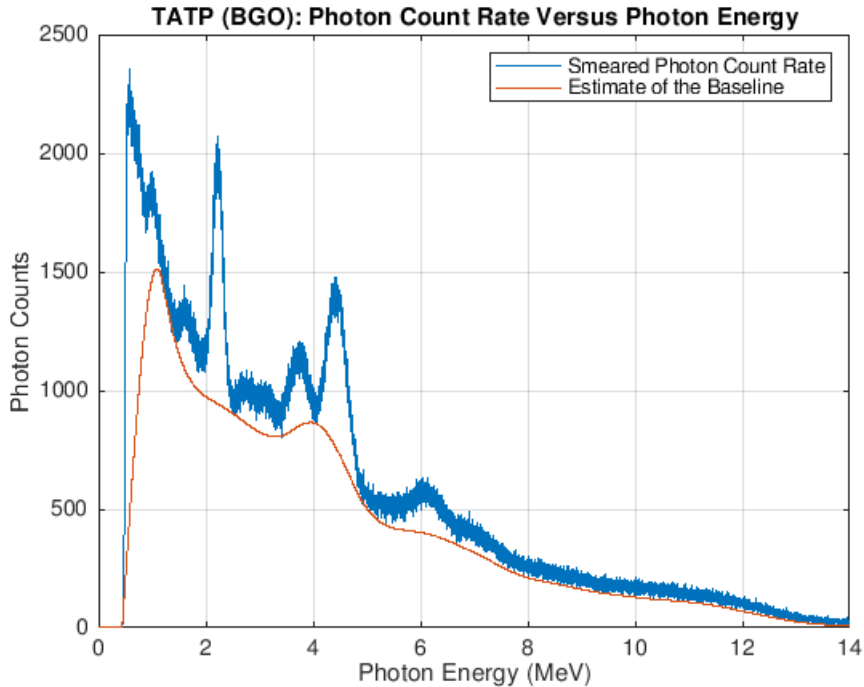
- the first estimate for the baseline is the signal itself;
- the weights are given the value of unity and a matrix equation, which is associated with this minimisation problem [56], is solved to give a first estimate of the baseline;
- the weights are recalculated according to the value of the parameter p and the matrix equation is resolved to find another estimate of the baseline;
- the preceding step is repeated until the baseline estimate converges.

It has been determined that just ten iterations of these steps were enough for the baseline to converge to an accurate estimate [56]; hence, after verifying this finding with our data, it was chosen that this iteration number would be used in all subsequent estimates of the baselines for the gamma spectra. Implementing this algorithm for the spectrum given in Fig. 12 obtained an estimate of the baseline that is shown in Fig. 13.

This is demonstrably not an accurate estimate of the baseline for this spectrum: specifically, by visual inspection of Fig. 13, it is clear that it doesn't closely fit the signal at lower photon energies ($\lesssim 1\text{MeV}$). This could not be improved by decreasing the parameter p , which would have had the effect of the baseline more closely fitting the data, because it would also lead to the baseline more closely fitting the peaks in the spectrum, which would not be ideal for obvious reasons. Hence, a more ad hoc approach was needed to both accurately estimate the baseline at lower energies and also to not effect it at higher energies where a lot of the characteristic gamma-ray peaks are found. Two of the following approaches were tested and their estimates of the baseline were visually compared against each other:

- determine the photon energy at which the peak in the “background” from the spectrum of smeared photon counts occurs, and then only use the data above this energy when calculating the baseline;

Figure 13: A plot of the photon counts against the energy of the photons for TATP along with an estimate of the baseline using the parameters $p = 10^{-5}$ and $\lambda = 10^6$.



- similarly determine the photon energy and photon count at the peak in the “background”, but instead of discarding the data as in the previous approach, assign this value to all energy bins situated at lower energies than this peak. Next, make an estimate of the baseline using this adjusted spectrum and then discard the data below the peak energy.

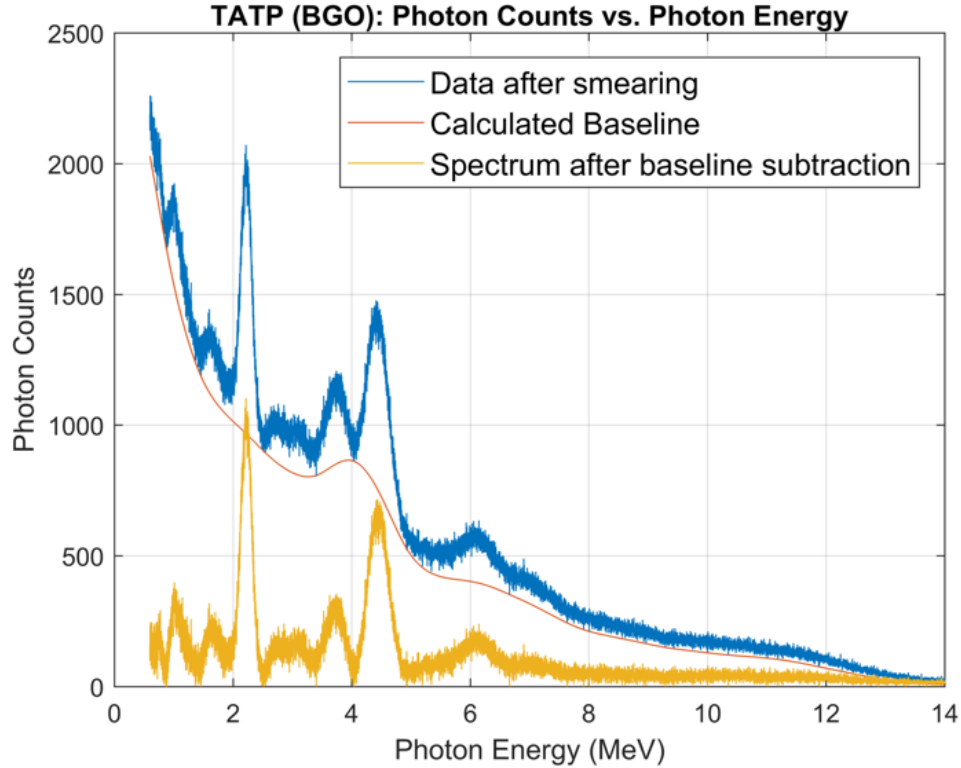
It was found that the second approach was best for accurately representing the true baseline of the gamma spectra; this is probably due to the fact that by increasing the signal strengths at the lower energies it managed to force the ASL algorithm to more closely fit the spectrum at these energies. An improved estimate of the baseline using this approach is shown in Fig. 14.

The peak in the baseline occurred at less than 0.6005MeV and 0.5055MeV for the BGO and HPGe detectors respectively; hence, in order to keep the domain of the spectra of each detector the same, the data at energies below these two energies were discarded for all of the spectra that were simulated. The baseline obtained for TATP using the HPGe detector is shown in Fig. 15. The optimum values for the p and λ parameters for HPGe were found to be 10^{-4} and 10^5 respectively.

3.4 Artificial Neural Network (ANN)

The relationship between the photon counts as a function of energy in spectra obtained using neutron activation and the elemental compositions of the assayed samples is complicated. In order to theoretically determine the composition, the following information would have to be known: the transmission of the neutrons to the voxel where scattering has taken place; the differential cross section for inelastic neutron scattering; and the transmission of the emitted photons from the place of

Figure 14: A plot showing the improved estimate of the baseline for TATP; the baseline has been subtracted from the smeared photon counts to determine the photon counts belonging to each characteristic peak (yellow).

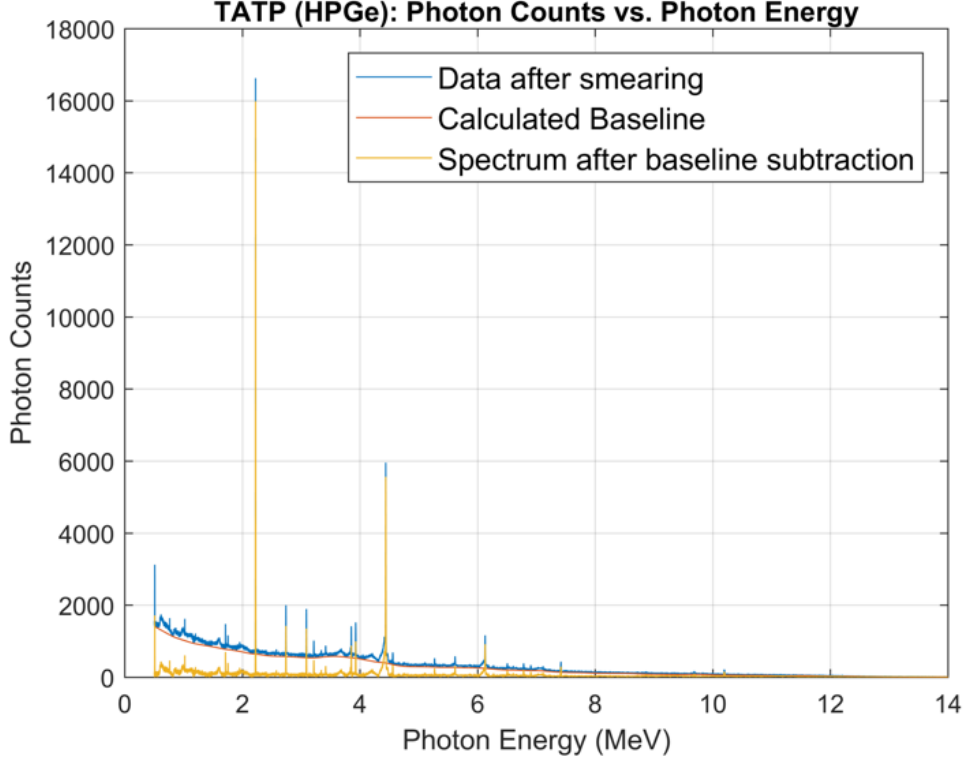


scattering to the point of detection. The fact that all these parameters are dependent on which nuclei are within the sample leads to a logical loop: information on the elemental composition of an unseen sample is needed in order to determine the composition of the sample. Hence, other methods for determining the composition of the sample from its gamma spectrum need to be developed. It is proposed that the use of an artificial neural network (ANN) that has been trained with gamma spectra obtained from “seen” samples, i.e., the elemental composition of these samples is revealed to the ANN, could be a possible solution. If enough gamma spectra are used to train it, then it is perhaps possible to develop a detection system that can determine the compositions of samples with enough accuracy to be able to discriminate between explosives and benign material. The ANN developed for this study has been coded in Python using the open source Keras and Tensorflow libraries; its structure included the following general features:

- an input layer with the same number of nodes as the number of energy bins included from the multi-channel pulse height analyser- each node takes the value of the photon count of one of the energy bins;
- three hidden layers in which the nodes in each layer are fully connected to the nodes in the previous layer and similarly to those in the successive layer. The connections between nodes are weighted such that the value of a node is the weighted sum of the values of the nodes in the previous layer;
- An output layer consisting of 4 nodes which represent the percentage compositions of Hydrogen, Nitrogen, Carbon and Oxygen in the sample.

In the training phase of development, gamma spectra from 65 fictitious materials (see

Figure 15: The gamma spectrum for TATP using the HPGe detector; the baseline has been determined and subtracted from the smeared photon counts to give an estimate of the photon counts for the characteristic peaks (yellow).



Appendix 7.3) were used to train the ANN; these covered the full 4-dimensional space of H, C, N and O percentage compositions- this was done so that it was prepared for estimating the composition of any sample containing only these four elements, which happens to be most explosives. The ANN then adjusted the matrix of weights in the network to minimise a loss function for the error in the predicted values of the percentage compositions. The ANN was trained and optimised separately for the BGO and HPGe detectors- the optimised number of nodes in each layer of the ANN for the two detectors is shown in Table 1.

	BGO	HPGe
Input nodes	670	15
Nodes in 1 st layer	670	50
Nodes in 2 nd layer	1340	100
Nodes in 3 rd layer	670	50

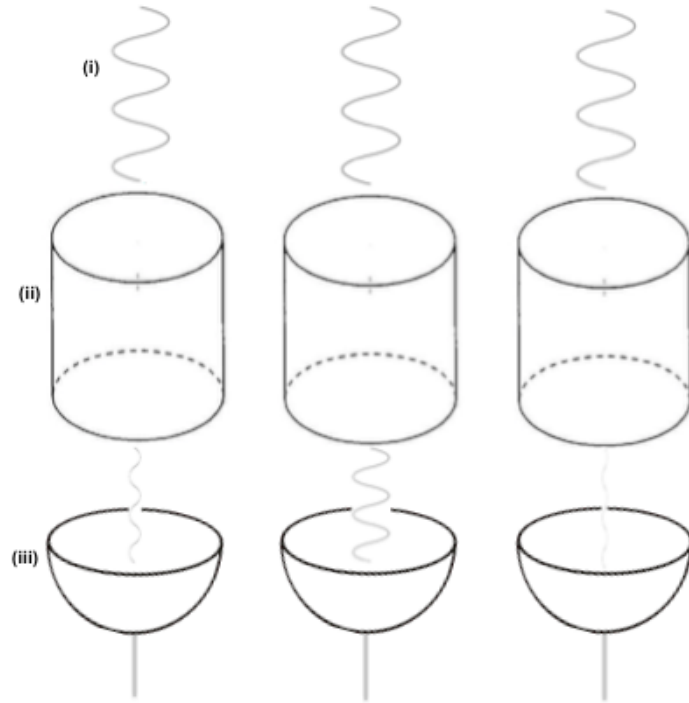
Table 1: The optimised structure of the ANN for gamma spectra obtained using the BGO and HPGe detectors.

4 Analysis

4.1 Chromatic Detection Technique: Using Spectrum Filters

As discussed in section 2.3, it was hypothesised that the use of spectrum filters with different transmission curves could be used to determine the elemental composition of an assayed sample. The proposition was to place filters in front of the gamma-ray detectors so as to change their spectral response functions. There would need to be several gamma-ray detectors, each with a spectrum filter, so that the ratio between the intensity of radiation which is incident on each of them could be used to extract information about the composition of the sample that is emitting such radiation (see Fig. 16 for clarification on how the detectors and spectrum filters would be configured for an explosive detection system).

Figure 16: A configuration of three gamma-ray detectors (iii) and three different spectrum filters (ii); the filters alter the intensity of radiation (i) that is incident on the detectors and thus their spectral response functions.



In order to verify whether this approach would work it was necessary to meticulously investigate the total absorption cross sections, $\sigma(E)$, for all materials that were possible candidates as spectrum filters. To restrict our research to only those materials that could practically be used in a real-world explosive detection system, we precluded materials in which one or more of the following applied:

- it is not a solid at room temperature and pressure,
- the material is radioactive and would therefore pose a health and safety threat,
- it is prohibitively expensive and/or is in short supply.

The second prerequisite led to the preclusion of all those elements with an atomic mass of $Z \geq 83$. In the end, the total absorption cross sections of 28 elements, ranging from $Z = 13$ to $Z = 83$, were analysed using tabulated data found in the

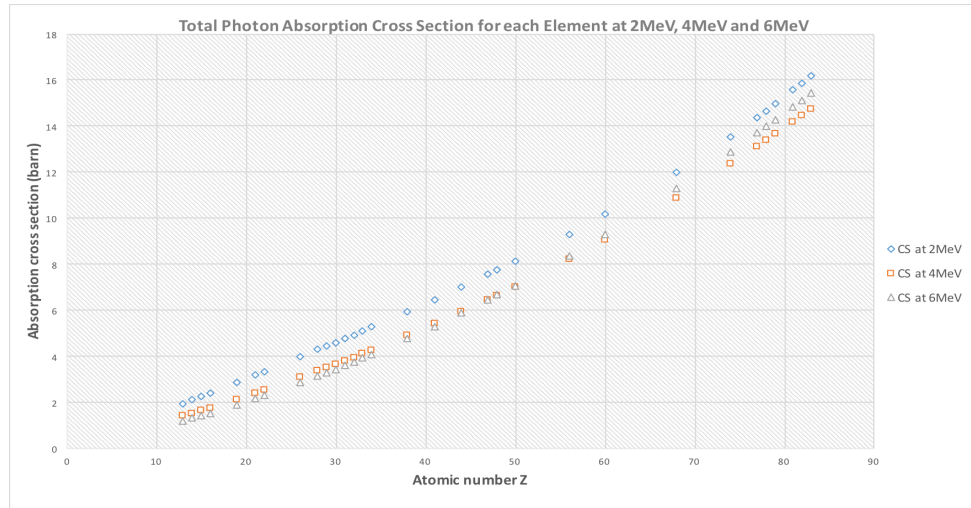
literature (see Appendix 7.5). As the characteristic gamma rays were predominantly in the range of 2-6MeV, our analysis focused on the cross sections at three photon energies: 2MeV, 4MeV and 6MeV.

An effective spectrum filter is one that transmits photons with one of these energies more than the others whilst also not significantly reducing the intensity of incident radiation: therefore, for each filter, the thickness, x , required such that the ratio between the transmittance at two of the aforementioned photon energies is N was calculated. Using equation 13 from section 2.8, it can be shown that given two photon energies the thickness of the filter that satisfies this condition is given by:

$$x = \frac{\ln N}{|n(\sigma(E_1) - \sigma(E_2))|}, \quad (17)$$

where n is the number density of the material; and $\sigma(E_1)$ and $\sigma(E_2)$ are the total photon absorption cross sections at energies E_1 and E_2 respectively. Furthermore, as the cross sections at more than two energies were being investigated and also that a spectrum filter would be deemed suitable for transmitting photons that had the greatest transmittance through the material, the values used for the cross sections in equation 13 were the two smallest amongst the three photon energies considered. It was discovered that the cross section of filters with an atomic mass between $Z = 13$ and $Z = 47$ was smallest for the 4MeV photons, whereas for filters between $Z = 48$ and $Z = 83$ it was smallest for 6MeV photons (see Fig 17). Hence, the former can be labelled as being suitable for the discrimination of photons centred around 4MeV and the latter for photons centred around 6MeV. The cross sections for the 2MeV photons were always the highest amongst the three energies and therefore no filter, by itself, could be labelled as being suitable for the discrimination of photons with energies around 2MeV. The thickness for each filter was then calculated using the aforementioned criteria and plotted as a function of the atomic mass (see Fig. 19).

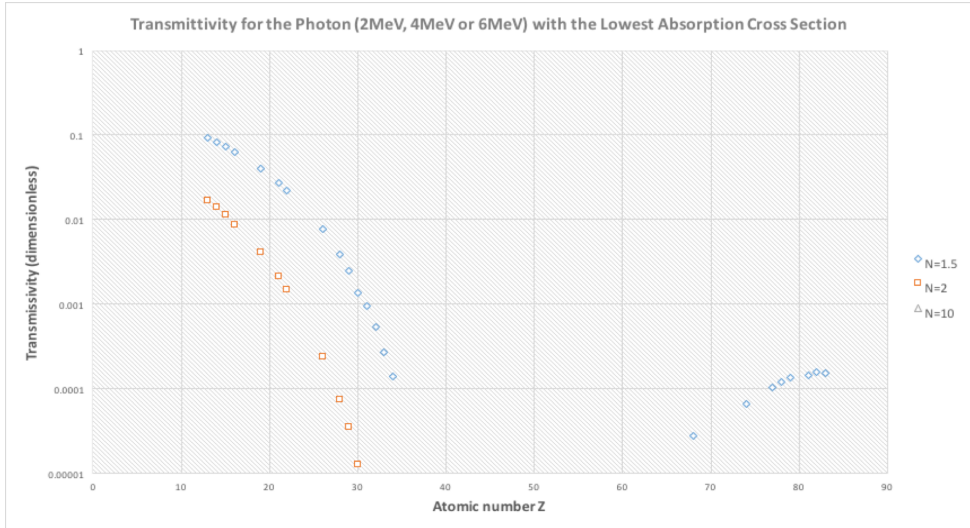
Figure 17: A plot of the total absorption photon cross sections for each element for 2MeV, 4MeV and 6MeV photons.



It can be clearly seen from Fig. 19 that the required thickness of the spectrum filters peaks at an atomic mass of $Z = 48$ (Cadmium) and that the thicknesses of many of the filters- especially those centred around the peak- are prohibitively large with some of them being several metres thick; as constructing such a large filter would be beyond practical they can no longer be considered as candidates for a spectrum filter in an explosive detection system.

Another criteria for an effective filter beyond the discrimination of photons based on their energy is that the filter has a sufficiently high enough transmittance such that the flux of photons reaching the detector is not comparable to statistical fluctuations. Hence, to determine whether any of the filters meet this criteria it was necessary to calculate their transmittance through a layer of homogeneous material- this was done using the thicknesses calculated above for $N = 1.5, 2$ and 10 and was plotted against the atomic mass of the filter (see Fig. 18).

Figure 18: A logarithmic plot of the transmittance through the filters for $N = 1.5, 2$ and 10 as a function of atomic mass. For $Z \leq 47$ the transmittances have been determined for 4MeV photons whereas for $Z \geq 48$ the 6MeV photons have been used. Transmittivities below 10^{-5} have not been plotted.



From Fig. 18, it is clear from the fact that the majority of the transmittances are exponentially small, that the intensity detected by the gamma-ray detectors could not be distinguished from background noise. The transmittance is only greater than 10^{-2} for filters with $Z \leq 22$ for $N = 1.5$ and for $Z \leq 15$ for $N=2$. The largest transmittance for $N = 10$ is for Aluminium ($Z = 13$) and has a value of 1.26×10^{-6} ; thus, it is clear that no filter with $N = 10$ exists such that it simultaneously satisfies the requirements of being both practical to build and also having a sufficiently high transmittance for the photons that it would like to pass through. Consequently, all materials except those specified above would not be viable for use as spectrum filters in an explosive detection system.

One of the ideal characteristics of a spectrum filter is that it has a narrow window of energy acceptance and as a result it is an effective discriminator of photon energies. To measure this one can define a function, ξ , which is equal to the fraction of photons transmitted with energies within the desired range of accepted energies compared to the total number of photons transmitted. As our analysis has only focused on cross section data at specific energies, the equation for ξ can be simplified to:

$$\xi_{4,6} = \frac{T_{4,6}}{T_2 + T_4 + T_6}, \quad (18)$$

where T is the transmittance and the subscripts relate to the 2MeV , 4MeV and 6MeV ; hence, $\xi_{4,6}$ are for the filters that are suitable for the 4MeV and 6MeV photons respectively. ξ was plotted as a function of Z for $N = 1.5, 2$ and 10 (see Fig. 20).

Figure 19: A logarithmic plot of the thickness (cm) required for a filter to produce a difference in the transmittance between the photon energies corresponding to the two lowest cross sections of a multiplicative factor of N . The thickness has been calculated for $N = 1.5, 2$ and 10 .

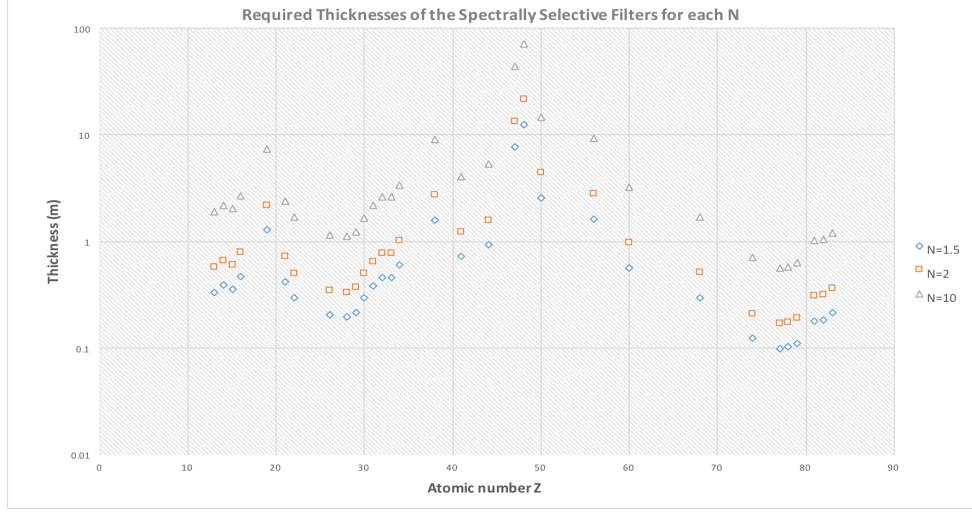
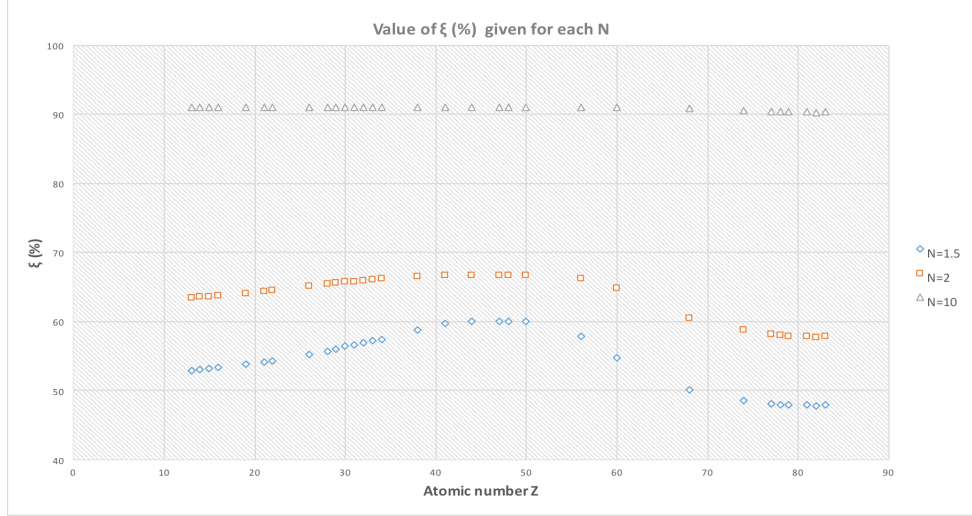


Figure 20: ξ is plotted for all filters for $N = 1.5, 2$ and 10 .



By considering only filters with $Z \leq 22$ for $N = 1.5$ and $Z \leq 15$ for $N = 2$, it is found that $\xi_6 \leq 0.543$ for the former and $\xi_6 \leq 0.636$ for the latter. This means that a large fraction of the photons that are transmitted through the filter are not those corresponding to 6MeV photons. Furthermore, as we have only considered photons with energies of 2MeV, 4MeV and 6MeV, it is evident that in a real world application of such a filter ξ would be much lower. Hence, there are no filters that can be proposed for use in a explosive detection system based on the trichromatic approach. Until such filters can be built this technology will be unable to progress to the next stage of development.

4.2 Bismuth Germanate (BGO) Detector

The gamma spectra obtained from the Geant4 simulations with the BGO detector were Gaussian smeared with a constant resolution of 10%, as discussed in section 3.2. Such a resolution, which is of the same order of magnitude as most scintillator-

based detectors [52], meant that many of the characteristic gamma-ray peaks corresponding to the emissions of Hydrogen, Carbon, Nitrogen and Oxygen could not be resolved. Hence, instead of isolating each of the characteristic peaks in the gamma spectra and taking the inputs of the ANN as the photon counts within some range of photon energies centred at each of the photopeaks, it was instead decided that the inputs to the ANN should include all photon counts between the energies of 0.6005MeV and 14MeV- the former being the value where the ALS method breaks down due to the use of a more ad hoc approach to determining the baseline (see section 3.3). The gamma spectra can thus be split into bins of photon energies between these two extrema by using multi-channel pulse height analysers. The widths of the energy bins can be adjusted so as to optimise the accuracy of the predictions of the ANN: a bin width that is too large will lose some of the information contained within the gamma spectra but reduce the computational load, whereas one that is too small will have larger statistical fluctuations on the photon counts of each bin and will increase the computational load. The bin widths that were used to test the predictive capabilities of the ANN were 1KeV, 5KeV, 20KeV and 50KeV.

4.3 High Purity Germanium (HPGe) Detector

As mentioned in section 3.2, the gamma spectra obtained using the HPGe detector had much better resolution than those using the BGO detector. For instance, at the energy corresponding to the dominant characteristic gamma-ray emission of Oxygen, i.e, 4.44MeV, the resolutions of the two detectors were modelled as 0.13% and 10% respectively. These resolutions translated into characteristic gamma-ray peaks with FWHMs of 6KeV for the HPGe detector and 0.44MeV for the BGO detector- this is a direct manifestation of the narrow band gap of HPGe (see section 2.5). Hence, unlike the gamma spectra obtained using the BGO detectors, it was possible to resolve most of the characteristic gamma-ray peaks. The main peaks for each of these elements were obtained from the gamma spectra of the pure elemental samples using the HPGe detector. The photon energies corresponding to where each of the characteristic peaks, which numbered sixteen in total, began and ended- defined as a photon count approximately twice that of the baseline- was then systematically determined (see Table 2).

By inspecting Table 2, it is easy to verify that all bar two of the characteristic gamma-ray peaks could be resolved by the HPGe detector; the two peaks that could not be resolved- due to their lower and upper bounds overlapping- are the Carbon and Nitrogen characteristic emissions centred at 4.44MeV. Hence, the resolving power of the HPGe detectors is much greater than the BGO detectors, which should drastically improve the accuracy of the predictions of the elemental compositions of the unseen samples.

Due to the much improved resolution of the HPGe detector, it was decided that instead of using all the photon counts from 0.505MeV to 14MeV, the inputs to the ANN would be the photon counts within bins bounded by the photon energies of each of the characteristic gamma-ray peaks shown in Table 2. There were two reasons for using such an approach: firstly, including the photon counts at energies corresponding to none of the characteristic peaks is probably extraneous and would not likely improve the accuracy of the predictions; and secondly, because the peaks are more highly resolved, the photon counts away from these peaks are probably more influenced by the ALS smoothing than anything else, and therefore including this data would probably skew the predictions. Therefore, after merging the two

Table 2: A table showing the lower and upper bound photon energies of the characteristic gamma-ray peaks of Hydrogen, Carbon, Nitrogen and Oxygen. The widths, defined as the difference between the lower and upper bounds are also shown for each gamma-ray peak.

Element	Lower Bound (MeV)	Upper Bound (MeV)	Width of Peak (MeV)
H	2.219	2.23	0.011
C	3.212	3.218	0.006
	3.923	3.932	0.009
	4.434	4.443	0.009
N	0.726	0.731	0.005
	1.632	1.639	0.007
	2.309	2.317	0.008
	5.103	5.107	0.004
O	1.752	1.756	0.004
	2.738	2.745	0.007
	3.085	3.093	0.008
	3.836	3.843	0.007
	3.849	3.857	0.008
	4.433	4.443	0.01
	4.556	4.56	0.004
	6.123	6.134	0.011

unresolvable peaks into one energy bin, there were a total of fifteen energy bins which could be used as inputs to the ANN.

Using the gamma spectra of the 65 samples whose elemental compositions were known to the ANN as training data, it was then able to make predictions of the elemental compositions of the same 10 explosives and 10 benign materials used for the BGO detector.

4.4 Predictive Capabilities of the BGO and HPGe Detectors

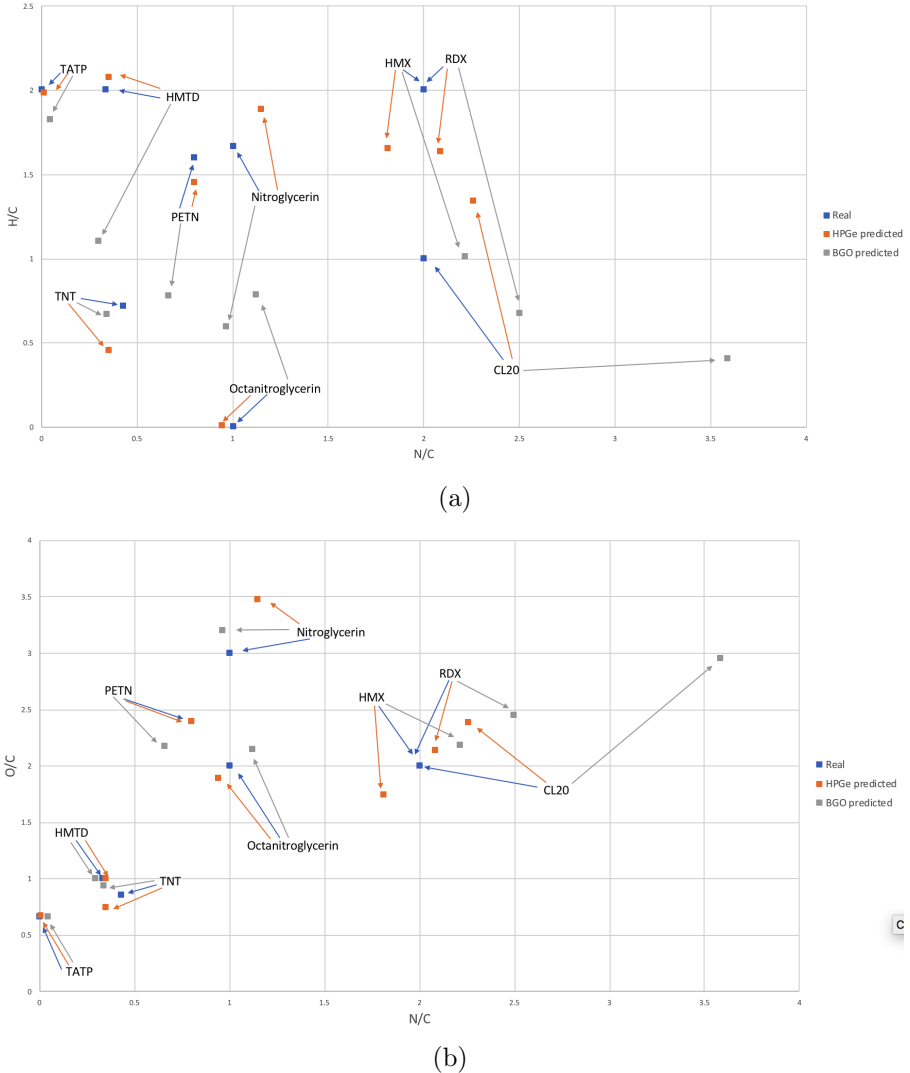
Using the gamma spectra obtained using the BGO and HPGe detectors as training sets, the ANN was then able to make predictions of the elemental compositions of the 10 explosives and 10 benign materials mentioned in section 4.2. The predictions for each of the unseen explosives are plotted as ratios of the percentage compositions of each of the elements (Hydrogen, Nitrogen and Oxygen) against the percentage composition of Carbon (see Fig. 21).

Fig. 21a and 21b are essentially the actual and predicted elemental compositions for the four elements for each of the 10 explosives, which are coordinates in 4-dimensional space, projected onto 2-dimensions. One can see just by visual inspection of the two plots that for most explosives the ANN gave better predictions for its elemental composition when using the HPGe detector. To quantify this further, one can define the error of the ANN predictions as the distance in 4-dimensional space from the actual to the predicted elemental compositions:

$$Error = \sqrt{\Delta H^2 + \Delta C^2 + \Delta N^2 + \Delta O^2}, \quad (19)$$

where ΔH is the difference between the predicted and actual composition of Hydrogen for a sample and the rest are likewise defined. Applying this to the predictions

Figure 21: Plots of the percentage compositions of Hydrogen (a) and Oxygen (b) against Nitrogen normalised by the percentage composition of Carbon for each of the unseen explosives. The actual compositions of the explosives as given by the PubChem chemical database are shown in blue; the predictions from the ANN using the HPGe and BGO detectors are shown in orange and silver respectively.



given by the ANN for the 10 explosives and 10 benign materials, it was found that the average error obtained when using the HPGe and BGO detectors were 0.125 ± 0.095 and 0.025 ± 0.021 respectively. It should be noted that the large variation in the error for the BGO detector is due to some of the predictions being much more inaccurate than 0.125. Hence, even though the errors obtained using the HPGe and BGO detectors overlap, one can still conclude that the predictive capabilities of the former are much greater than the latter. Moreover, if a comparison is made between the predictions using the two detectors (see Appendix 7.4), then in all bar one case, which is for TNT, the HPGe detector gave the best prediction of the elemental compositions. Therefore, we can conclude from this analysis that the HPGe detector would be better suited to the detection of explosives than the BGO detector. This was to be expected because the lower resolution of the BGO detector meant that more of the characteristic gamma-ray peaks could not be resolved compared to when using the HPGe detector, which would naturally reduce the predictive capabilities

of the detection system.

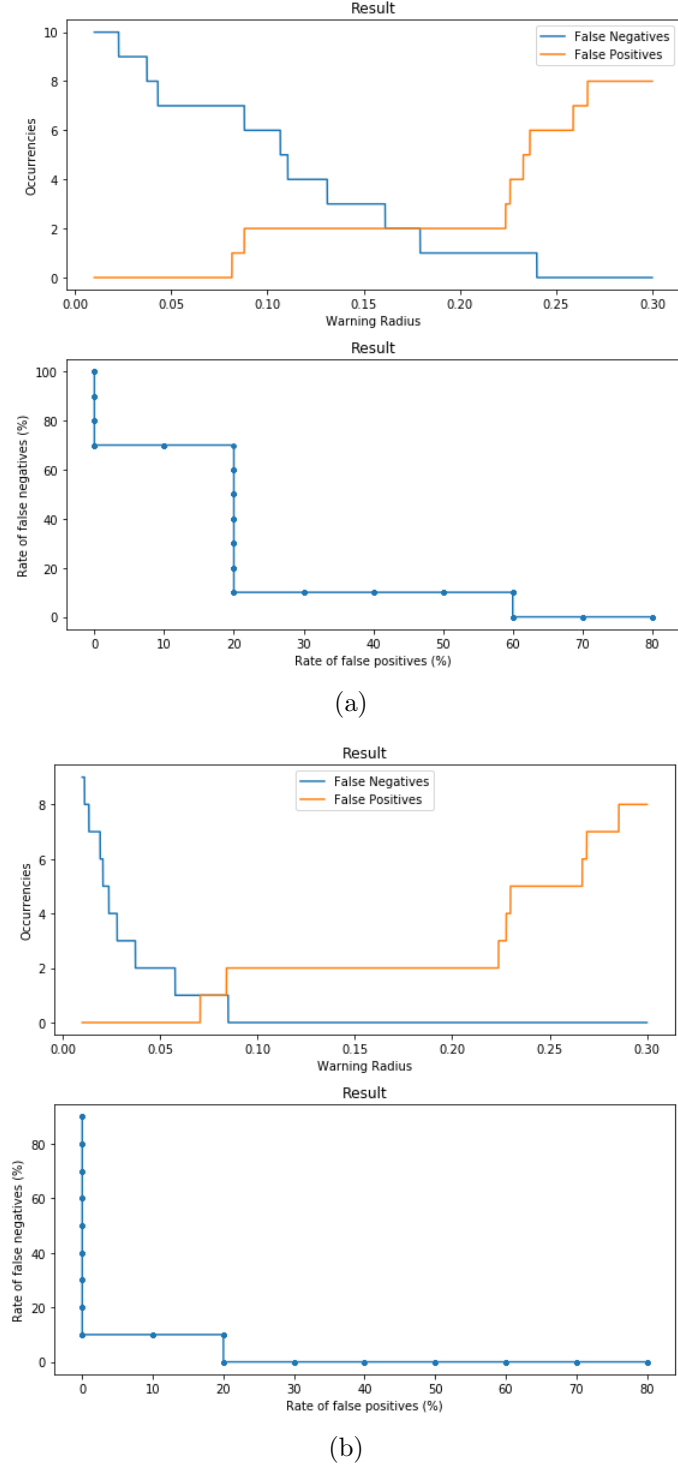
In order to compare the predictive capabilities of the ANN using both detectors to currently available detection technology, it is necessary to calculate a measure that would enable such comparison between vastly different systems. This comparison can be made by calculating the false positive and false negative rates for both detectors and then comparing them to the rates found in the literature for X-ray machines. Based on these detection rates, it would then be possible to make a comparison between the predictive capabilities of the two detection technologies and to make a final conclusion of whether the current generation of X-ray machines should be replaced, in the limited circumstances where enough shielding of the neutrons can be adequately provided, by a detection system based on neutron activation and gamma spectroscopy.

These detection rates have been calculated by defining a so-called “warning” radius, which can be imagined as the radius of a 4-sphere that is centred at each of the coordinates in the 4-dimensional space of the elemental compositions of Hydrogen, Carbon, Nitrogen and Oxygen corresponding to each of the 10 explosives. If the ANN gives a prediction that is within one of the 4-spheres for an explosive within our database, then a detection is made. A false positive is when the predicted elemental composition for a sample falls within the 4-sphere of an explosive when it is, in fact, not this explosive. Notice that this is a more rigorous definition of a false positive as it also includes the possibility of the ANN giving an inaccurate prediction of the elemental composition of an explosive but still falling within the 4-sphere of a different explosive that is in the database. A false negative is similarly defined as being when the predicted elemental composition of an explosive falls outside that of the 4-sphere of the same explosive in the database. As an ideal explosive detection system is one in which the false negatives are zero, it is necessary to set the warning radius at a value at which this is achieved and then to determine the false positive rate at which this occurs. The latter can then be used to make a comparison with other detection technology that are currently available and which are used specifically for the detection of explosives and contraband material. Fig. 22 shows the number of occurrences of false positive and false negatives as a function of the warning radius for the BGO and HPGe detectors and also plots the rate of false negatives against the rate of false positives as the warning radius is incrementally increased in steps of 10^{-5} .

The plots of the number of occurrences of false positives and false negatives as a function of warning radius are fairly intuitive: as the warning radius is increased, the predictions of the ANN are more likely to fall within the 4-spheres of the explosives in the database; therefore, whether or not the sample being assayed is an explosive or contraband material, it is more likely, all other things being constant, to be detected and, hence, the number of false negatives goes down and the number of false positives goes up. The value of the warning radius needed for the number of false negatives to be zero is a measure of the accuracy of the ANN predictions: one can see from Fig. 22a and 22b that a warning radius of 0.24 and 0.08494 is required for the BGO and HPGe detectors respectively; this is another indication that the predictive capabilities of the detection system are much greater when using the HPGe detector. Furthermore, the rate of false positives needed for the rate of false negatives to be zero is 60% when using the BGO detector and 20% when using the HPGe detector. Hence, if this detection system, i.e., one relying on neutron activation and gamma spectroscopy, was implemented in the real-world, the one using HPGe detectors would have a much lower false detection rate and, therefore, it would require fewer instances of having to do further checks on the sample to verify

the threat level that it poses. If these detection rates are compared to those found using CT X-ray imaging, such as the CTX-5000, which is an automatic explosive detection system developed by inVision Technologies and was the first to be certified by the US Federal Aviation Administration (FAA) in 1994 [57, 58], then one would find that the false positive rates of such detection systems (CTX-5000) are around 30% [57]. Such a rate of false positives has been found to lead to significant delays for air passengers as it could only process between 150-200 bags per hour in real-world conditions [59]. Hence, we can confidently conclude that the false positive rate found for neutron activation and gamma spectroscopy using the BGO detector would be prohibitively high and should not therefore be recommended as a replacement of the current generation of explosive detection technology. The rate of false positives determined for the HPGe detector are lower (20% compared to the 30% found for the CTX-5000) but this false detection rate was determined in an idealised detection environment, i.e., there was no shielding and the sample was modelled as a simple spherical shell surrounded by a vacuum (see section 3.2); hence, it is likely that the false positive rate that it gives in real-world conditions would be much greater than this. Moreover, if the extra operating costs of such an explosive detection system are considered, which would be much greater because of the requirement for the HPGe detectors to be constantly cooled with liquid nitrogen coolant, then it is more reason to conclude that the use of neutron activation and gamma spectroscopy would not provide any solutions to the problems faced by the current generation of explosive detection technology.

Figure 22: A plot of the number of occurrences of false positives and false negatives as a function of the trigger radius for the BGO (a) and HPGe (b) detectors. The rate of false negatives is also plotted against the rate of false positives in increments of 10^{-5} in the trigger radius.



5 Conclusion

The main objective of this study was to assess the possibility of using neutron activation and gamma spectroscopy as a replacement for X-ray imaging for the detection of explosives. The failure of the latter to discriminate between a plastic explosive and other substances with similar X-ray absorption coefficients [4] means that an alternative detection technology, which is based on different physics, is required if governments around the world want to be able to thwart the increasing threat posed by international terrorism. The use of neutron activation and gamma spectroscopy as an alternative explosive detection technology has been investigated with two methods for discriminating between substances with different elemental compositions being evaluated. The first approach, which envisioned using spectrally selective filters in a similar way to how the human eye discriminates between different colours, was found to be unfeasible. The main reason for this was that no spectrum filter could be found which provided enough selectivity between photons with energies in the 2-6MeV range. An alternative approach using an ANN to discriminate between gamma spectra of samples with different elemental compositions has also been tested. The neutron interrogation of samples along with the detection by BGO and HPGe detectors of the emitted gamma-ray photons has been successfully modelled in Geant4 and the gamma spectra obtained has been used to train and test the ANN. The predictive capabilities of the ANN using the BGO detector has been found to be inadequate due to the high false positive rates obtained (60%). The use of HPGe detectors to discriminate between explosives and benign materials has been found to be more promising, with a false positive rate of 20%. Further research would, however, be needed to ascertain the kind of detection rates that this system would obtain in more realistic environments. For instance, it is recommended that future research include the following improvements to the computational models:

- more realistic samples with non-homogeneous compositions and the use of scattering angle data to provide a computed tomographic image;
- simulate the effects of including shielding material around the detector to investigate to what extent this affects the detection rates;
- model the time resolution of the detectors in order to include the coincident photon peaks in the gamma spectra- this is likely to reduce the predictive capabilities of the detection system as some peaks are at double the energy of the dominant 2.22MeV Hydrogen peak;
- take into account the distribution of the elemental compositions of different explosives.

The last recommendation could perhaps be implemented by changing from a constant warning radius to a unique detection volume for each explosive in the database. Finally, the health and safety implication of using fast neutrons needs to be considered as they are highly penetrative and, thus, can pose a danger to the health of both the public and the operators of the detection system.

6 Acknowledgements

I would first like to thank my MSci project partner whose strong work ethic throughout the project and his excellent scientific knowledge propelled the project forward. Without a doubt we would not have achieved such a high standard of scientific rigour

if it were not for his involvement in the project. I would also like to acknowledge the help of another student, whose previous work on the same project [62] and his writing of the Geant4 simulation code laid the foundation for our research. Lastly, I wish to acknowledge the help that Dr Raymond Beuselinck gave us in order to understand how to use and navigate the computers in the High Energy Physics Department of Imperial College London.

References

- [1] Global Institute for Economics & Peace, (2017). Global Terrorism Index 2017.
- [2] (2017) Growth Opportunities in the Global Security Detection System Market [online]. Available at: <https://www.prnewswire.com/news-releases/global-security-detection-system-market-growth-opportunities-2017-2022—market-is-expected-to-reach-an-estimated-53-billion-300553060.html> [Accessed 15 April 2018].
- [3] National Consortium for the Study of Terrorism and Responses to Terrorism (START). (2017). Global Terrorism Database [Data file]. Available at: <https://www.start.umd.edu/gtd/> [Accessed 15 April 2018].
- [4] Zentai, G., 2008. X-ray imaging for homeland security. Imaging Systems and Techniques, 2008. IST 2008. IEEE International Workshop on, pp.16.
- [5] BBC Newsbeat, (2015). Computed tomography X-ray image of a bag [Online image]. Available at: <http://www.bbc.co.uk/newsbeat/article/34751690/how-airport-scanners-check-your-bag-is-safe-to-fly> [Accessed 15 April 2018].
- [6] Whetstone, Z., & Kearfott, D. (2014). A review of conventional explosives detection using active neutron interrogation. Journal of Radioanalytical and Nuclear Chemistry, 301(3), 629-639.
- [7] Randle, K., 1987. The applications of fast neutron activation analysis (FNAA) at Birmingham. Nuclear Inst. and Methods in Physics Research, B, 24(2), pp.10101013.
- [8] Yip, S. [online]. Interactions of Neutrons with Matter, Chapter VII. Available at: http://web.mit.edu/22.54/ClassNotes/22_111_VII.pdf [Accessed 11 Mar. 2018].
- [9] Atzeni, S. & Meyer-ter-Vehn, Jrgen, 2009. The physics of inertial fusion : beam plasma interaction, hydrodynamics, hot dense matter. Chapter 1: nuclear fusion reactions, Oxford: Oxford University Press.
- [10] Holmes, R.J. (1982). Gamma ray and neutron sources (AAEC/S-24). Sowerby, B.D. (Ed.). Australia. Available at: http://www.iaea.org/inis/collection/NCLCollectionStore/_Public/14/792/14792880.pdf [Accessed 16 March 2018].
- [11] Rinard, P, Neutron Interaction with Matter, in Passive Nondestructive Assay of Nuclear Materials, ed. by D. Reilly et al., U.S. Nuclear Regulatory Commission, NUREG/CR-5550, March 1991, p. 359-361.
- [12] Sakoda, A. et al., 2017. Production and detection of fission-induced neutrons following fast neutron direct interrogation to various dry materials containing ^{235}U . Journal of Nuclear Science and Technology, pp.19.
- [13] Schober, H., 2014. An introduction to the theory of nuclear neutron scattering in condensed matter. Institut Laue Langevin & Université Joseph Fourier [online]. Available at: <https://content.iospress.com/download/journal-of-neutron->

- research/jnr016?id=journal-of-neutron-research%2Fjnr016 [Accessed 24 April 2018].
- [14] Reilly, D., Ensslin, N., Smith, H. and Kreiner, S. (1991). Passive Nondestructive Assay of Nuclear Materials. Springfield, VA: US Department of Commerce, National Technical Information Service.
 - [15] Compton Scattering. (2017). [online]. Available at: https://casper.berkeley.edu/astrobaki/index.php/Compton_Scattering [Accessed 24 April 2018].
 - [16] Pair production. University of Florida [online]. Available at: https://www.astro.ufl.edu/~guzman/ast7939/glossary/pair_production.html [Accessed 24 April 2018].
 - [17] Wikimedia Commons, (2006). Diagram of Compton Scattering. [online] Available at: https://de.wikipedia.org/wiki/Datei:Compton_scattering-de.svg [Accessed 14 April 2018].
 - [18] Radiology Key, (2016). Scintillation and Semiconductor Detectors. [online] Available at: <https://radiologykey.com/scintillation-and-semiconductor-detectors/> [Accessed 5 Mar. 2018].
 - [19] Saha, G. (2006). Physics and Radiobiology of Nuclear Medicine. New York, NY: Springer New York. p.80-81.
 - [20] Majumdae, R.C., Mathur, V.S. & Dhar, J. (1959). Multiple photon production in Compton scattering and bremsstrahlung. Società Italiana di Fisica, Il Nuovo Cimento, Volume 12, Issue 2, pp 97105.
 - [21] ZIJP, W.L. (1984). Lecture Notes on Computerised Gamma-Ray Spectroscopy. Netherlands Energy Research Foundation. [online] Available at: http://www.iaea.org/inis/collection/NCLCollectionStore/_Public/15/042/15042453.pdf [Accessed 14 April 2018].
 - [22] Zmeskal, Z. (2015). Scintillators [PowerPoint Presentation]. VO 260 066: Detector and detector systems for particle and nuclear physics I. [online] Available at: https://www.oeaw.ac.at/fileadmin/subsites/etc/Institute/SMI/PDF/Detectors_WS2014-15_A2.pdf [Accessed 14 April 2018].
 - [23] Krammer, M. Scintillators [PowerPoint Presentation]. Detectors for Particle Physics. Institute of High Energy Physics, Vienna, Austria. [online] Available at: https://www.hephy.at/fileadmin/user_upload/VO-5-Scintillators.pdf [Accessed 14 April 2018].
 - [24] Wikimedia Commons, (2013). Schematic view of a photomultiplier coupled to a scintillator, illustrating detection of gamma rays. [online] Available at: <https://commons.wikimedia.org/wiki/File:PhotoMultiplierTubeAndScintillator.svg> [Accessed 14 April 2018].
 - [25] M. Rizzi, M. D'Aloia and B. Castagnolo, 2010. Semiconductor Detectors and Principles of Radiation-matter Interaction. Journal of Applied Sciences, 10: 3141-3155.
 - [26] Hastings, S. & Marcia, L. Gamma Spectroscopy, in Passive Nondestructive Assay of Nuclear Materials, ed. by D. Reilly et al., U.S. Nuclear Regulatory Commission, NUREG/CR-5550, March 1991, pp. 46-50.
 - [27] Scholze, F., Rabus, & Ulm. (1998). Mean energy required to produce an electron-hole pair in silicon for photons of energies between 50 and 1500 eV. Journal of Applied Physics, 84(5), 2926-2939.

- [28] Techniques for nuclear and particle Physics experiments: By W.R. Leo. (Springer, Berlin and Heidelberg, 1987) pp xvi 368, Soft cover, DM 80-. ISBN 3-540-17386-2. (1988). Nuclear Inst. and Methods in Physics Research, B, 34(2), 290.
- [29] Dendooven, P. Detection of Energetic Particles and Gamma Rays: Semiconductor Detectors [online]. Basic Detection Techniques (2009/2010). Available at: <http://www.astro.rug.nl/~peletier/Bas%20Det%20Tech%202009%20semiconductors.pdf> [Accessed 14 April 2018].
- [30] Leroy, C. (2010). Review of radiation detectors. AIP Conference Proceedings, 1204(1), pp.4957.
- [31] Kukk, E. (2011). UFYS3054: Radiation and particle detectors [Lecture Notes]. University of Turku. Available at: http://www.physics.ohio-state.edu/klaus/s12-780/references/turku_lecturenotes.pdf [Accessed 14 April 2018].
- [32] Klein, C.A. Bandgap dependence and related features of radiation ionization energies in semiconductors, J. Appl. Phys. 39 (1968) 20292038.
- [33] Kittel, C. & McEuen, Paul, 2005. Introduction to solid state physics 8th ed., New York; Chichester: Wiley. pp.205-206.
- [34] Precker J. W. & da Silva M. A., 2002. Experimental estimation of the band gap in silicon and germanium from the temperature-voltage curve of diode thermometers. Am. J. Phys. 70 1150-3.
- [35] Upp, D.L., Keyser, R.M. & Twomey, T.R., 2005. New cooling methods for HPGe detectors and associated electronics. Journal of Radioanalytical and Nuclear Chemistry, 264(1), pp.121126.
- [36] Med Phys 4RA3, 4RB3/6R03: Radioisotopes and Radiation Methodology. Chapter 5: Gamma-ray Spectrometry with Scintillators [online]. Available at: https://www.science.mcmaster.ca/radgrad/images/6R06CourseResources/4RA34RB3-Lecture_Note_5_Gamma-ray-Spectrometry.pdf [Accessed 24 April 2018].
- [37] Leclére, A-S., 2001. An evaluation of Bremsstrahlung cross-sections for keV to GeV electrons, Master of Science, University of Florida, Florida.
- [38] Yilmaz, E., 2003. Characteristic X-ray, Photoelectron, and Compton-Scattered Photon Escape from a HPGe Detector. Graduate School of Natural and Applied Sciences of the Middle East Technical University. Thesis [online]. Available at: <http://citeseerx.ist.psu.edu/viewdoc/download?doi=10.1.1.632.6314&rep=rep1&type=pdf> [Accessed 25 April 2018].
- [39] Liao, Y., 2006. Practical Electron Microscopy and Database. Comparison between EDS and AES. [online]. Available at: <http://www.globalsino.com/EM/page4660.html> [Accessed 25 April 2018].
- [40] Rittersdorf, I., 2007. Gamma Ray Spectroscopy. Nuclear Engineering & Radiological Sciences
- [41] Ortec, (2018). Single Channel Analyzers. [online] Available at: <http://www.ortec-online.com/products/electronics/single-channel-analyzers-sca> [Accessed 17 Jan. 2018].
- [42] Single-Channel Pulse-Height Analyzers. (2018). [ebook] Ortec. Available at: <http://122.physics.ucdavis.edu/course/cosmology/sites/default/files/files/Gamma%20Spec/PulseHeightAnalysis.pdf> [Accessed 23 Jan. 2018].

- [43] Young, T. The Bakerian Lecture: On the Theory of Light and Colours. Philosophical Transactions of the Royal Society of London, 1 January 1802, Vol.92, pp.12-48.
- [44] NIST Chemistry WebBook, NIST Standard Reference Database 8 (XGAM). XCOM: Photon Cross Sections Database. NIST, PML, Radiation Physics Division [online]. Available at: <https://www.nist.gov/pml/xcom-photon-cross-sections-database> [Accessed 25 April 2018].
- [45] Stockman, A. & Sharpe, L. Human cone spectral sensitivities: a progress report. Vision Research, 1998, Vol.38(21), pp.3193-3206.
- [46] Hayward, E., 1970. Photonuclear Reactions, Center for Radiation Research National Bureau of Standards Washington, D.C. 20234. [online]. Available at: <https://www.gpo.gov/fdsys/pkg/GOV PUB-C13-0c46d22d2b1bf546a4752e467755ec0b/pdf/GOV PUB-C13-0c46d22d2b1bf546a4752e467755ec0b.pdf>
- [47] Geant4: A Simulation Toolkit. CERN, Switzerland, (2018). [online]. Available at: <http://geant4.web.cern.ch> [Accessed 25 April 2018].
- [48] National Center for Biotechnology Information. PubChem Compound Database; CID=129627851. [online] Available at: <https://pubchem.ncbi.nlm.nih.gov/compound/129627851> [Accessed 13 April 2018].
- [49] Crystals.saint-gobain.com. BGO Bismuth Germanate Bi₄Ge₃O₁₂. Products. Saint-Gobain Crystals. [online] Available at: <https://www.crystals.saint-gobain.com/products/bgo> [Accessed 13 April 2018].
- [50] Colosimo, S., & Boston, Andrew; Boston, Helen. (2013). The Characterisation of AGATA High Purity Germanium Detectors for Pulse Shape Analysis.
- [51] Matyàš, R., Pachman, J., 2013. Primary Explosives, Properties of Primary Explosives. Springer. pp.11-13.
- [52] Khodyuk, I.V. & Dorenbos, P., 2012. Trends and Patterns of Scintillator Non-proportionality. IEEE Transactions on Nuclear Science, 59(6), pp.3320-3331.
- [53] Calligaris, L., Massironi, A., & Presotto, L. (2006/2007). Gamma Spectroscopy. [online] Available at: https://www.google.co.uk/url?sa=t&rct=j&q=&esrc=s&source=web&cd=1&ved=0ahUKEwjYv8aXvbjaAhXBDMAKHT9hCzkQFggqMAA&url=http%3A%2F%2Fvirgilio.mib.infn.it%2Flabdida%2Flib%2Fexe%2Ffetch.php%3Fid%3Dlaboratorio_di_fisica_delle_particelle%26cache%3Dcache%26media%3Drelazionelaboratoriogamma.pdf&usg=AOvVaw1AMKc2-U03euox9gal2QFI [Accessed 14 April 2018].
- [54] Hueso-Gonzlez, F., Bemmerer, D., Berthel, M., Biegun, A.K., Borany, J.V., Dendooven, P., . . . Pausch, G. (2014). 90: Comparison of Scintillation Detectors based on BGO and LSO for Prompt Gamma Imaging in Particle Therapy. Radiotherapy and Oncology, 110, S44.
- [55] Nicolas, P., Chapter VIII: Detectors based on ionization in semiconductors, Universit libre de Bruxelles. [online]. Available at: http://metronu.ulb.ac.be/npauly/Pauly/metronu/10%20Part%202_3.pdf [Accessed 25 April 2018].
- [56] Eilers, P. & Boelens H. (2005). Baseline Correction with Asymmetric Least Squares Smoothing. Biosystems Data Analysis Group, Swammerdam Institute for Life Sciences (SILS), University of Amsterdam. Available at:

- https://zanran_storage.s3.amazonaws.com/www.science.uva.nl/ContentPages/443199618.pdf [Accessed 17 March 2018].
- [57] Wells, & Bradley. (2012). A review of X-ray explosives detection techniques for checked baggage. *Applied Radiation and Isotopes*, 70(8), 1729-1746.
 - [58] Committee on Commerce, Science and Transportation, (1997). Aviation Safety: Hearing Before the Subcommittee on Aviation of the Committee on Commerce, Science and Transportation, United States Senate. One Hundred Fifth Congress. First Session, March 5, 1997. p. 98.
 - [59] Butler. V & Poole, R. W. (2002). Rethinking Checked Baggage Screening. Reason Public Policy Institute, Reason Foundation.
 - [60] Young, T. The Bakerian Lecture: On the Theory of Light and Colours. *Philosophical Transactions of the Royal Society of London*, 1 January 1802, Vol.92, pp.12-48.
 - [61] Hubbell, J. et al., 1980. Pair, Triplet, and Total Atomic Cross Sections (and Mass Attenuation Coefficients) for 1 MeV-100 GeV Photons in Elements Z=1 to 100. *Journal of Physical and Chemical Reference Data*, 9(4), pp.10231148.
 - [62] Fan, T. (2017). Neutron Activation and Material Composition Analysis with Sodium Iodide and Polyvinyl Toluene Scintillators. Imperial College London. BSc Project Thesis.

7 Appendix

7.1 Substances Simulated in Geant4

Table 3: Chemical formulae and elemental compositions of the 10 explosives and 10 benign materials that were used in the Geant4 simulations.

	Material Name	Chemical Formula	Percentage Composition			
			H (%)	C (%)	N (%)	O (%)
Explosives	Ammonium Nitrate	$\text{H}_4\text{N}_2\text{O}_3$	44.4	0	22.2	33.3
	CL20	$\text{H}_6\text{C}_6\text{N}_{12}\text{O}_{12}$	16.7	16.7	33.3	33.3
	HMTD	$\text{H}_{12}\text{C}_6\text{N}_2\text{O}_6$	46.2	23.1	7.7	23.1
	HMX	$\text{H}_8\text{C}_4\text{N}_8\text{O}_8$	28.6	14.3	28.6	28.6
	Nitroglycerin	$\text{H}_5\text{C}_3\text{N}_3\text{O}_9$	25.0	15.0	15.0	45.0
	Octanitroglycerin	$\text{C}_8\text{N}_8\text{O}_{16}$	0.0	25.0	25.0	50.0
	RDX	$\text{H}_6\text{C}_3\text{N}_6\text{O}_6$	28.6	14.3	28.6	28.6
	PETN	$\text{H}_8\text{C}_5\text{N}_4\text{O}_{12}$	27.6	17.2	13.8	41.4
	TATP	$\text{H}_{18}\text{C}_9\text{O}_6$	54.5	27.3	0.0	18.2
	TNT	$\text{H}_5\text{C}_7\text{N}_3\text{O}_6$	23.8	33.3	14.3	28.6
Benign Materials	Benzodiazepine	$\text{H}_8\text{C}_9\text{N}_2$	42.1	47.4	10.5	0.0
	Perspex	$\text{H}_8\text{C}_5\text{O}_2$	53.3	33.3	0.0	13.3
	Melamine	$\text{H}_6\text{C}_3\text{N}_6\text{O}_6$	40.0	20.0	40.0	0
	Polybutadiene	$(\text{H}_6\text{C}_4)_n$	60.0	40.0	0.0	0.0
	Nitric Acid	HNO_3	20.0	0	20.0	60.0
	Sucrose	$\text{H}_{22}\text{C}_{12}\text{O}_{11}$	48.9	26.7	0.0	18.2
	PET	$\text{H}_8\text{C}_{10}\text{O}_4$	66.7	33.3	0.0	0.0
	Polypropylene	$(\text{H}_6\text{C}_3)_n$	66.7	33.3	0.0	0.0
	Polyethylene	$(\text{H}_4\text{C}_2)_n$	46.2	23.1	7.7	23.1
	2-4-4-Trimethylpentane	H_{18}C_6	75.0	25.0	0.0	0.0

7.2 Modelling the Resolution of the HPGe Detector

The HPGe detector has been modelled using a Gaussian smear with the following resolution function, $R(E)$, [53]:

$$R(E) = \sqrt{a^2 + \frac{b^2}{E} + \left(\frac{c}{E}\right)^2}, \quad (20)$$

$$a = 0.00113 \pm 0.00003,$$

$$b = 0.043 \pm 0.0013 \cdot \sqrt{E},$$

$$c = 1.23 \pm 0.01 \cdot E,$$

where E is the energy of the incident photon in units of KeV.

7.3 Composition of Fictitious Materials

Table 4: A table of the 65 fictitious materials used to train the ANN for both the BGO and HPGe detectors. 56 of the fictitious materials had elemental compositions that were equally spaced- with intervals of 20%- in the 4-dimensional space of Hydrogen, Carbon, Nitrogen and Oxygen percentage compositions. The rest were given compositions that were within 5% of the percentage compositions of the 10 explosives.

H(%)	C(%)	N(%)	O(%)	H(%)	C(%)	N(%)	O(%)
0	0	0	100	20	40	40	0
0	0	100	0	20	40	40	0
0	0	20	80	20	60	0	20
0	0	40	60	20	80	0	0
0	0	60	40	40	0	0	60
0	0	80	20	40	0	20	40
0	100	0	0	40	0	40	20
0	20	0	80	40	0	60	0
0	20	20	60	40	20	0	40
0	20	40	40	40	20	20	20
0	20	60	20	0	20	80	0
0	40	0	60	40	40	0	20
0	40	20	40	40	40	0	20
0	40	40	20	40	60	0	0
0	40	60	0	60	0	0	40
0	60	0	40	60	0	20	20
0	60	20	20	60	0	40	0
0	60	40	0	60	20	0	20
0	80	0	20	60	20	20	0
0	80	20	0	60	40	0	0
100	0	0	0	80	0	0	20
20	0	0	80	80	0	20	0
20	0	20	60	80	20	0	0
20	0	40	40	0	25	50	25
20	0	60	20	20	20	30	30
20	0	80	0	25	15	45	15
20	20	0	60	25	30	30	15
20	20	20	40	30	10	30	15
20	20	40	20	30	20	40	10
20	20	60	0	45	0	35	20
20	40	0	40	45	25	25	5
20	40	20	20	55	25	20	0
20	60	20	0				

7.4 ANN Predictions Using BGO and HPGe Detectors

Compound	REAL COMPOSITION			KERAS AVERAGE BGO 20keV			KERAS AVERAGE HPGe 15 bins			Error
	H (%)	C (%)	N (%)	O (%)	H (%)	C (%)	N (%)	O (%)	Error	
Ammonium Nitrate	44.4	0.0	22.2	33.3	12.6	0.5	36.2	50.4	38.8	43.3
CL20	16.7	16.7	33.3	33.3	5.1	12.8	45.7	37.7	17.9	19.3
HMTD	46.2	23.1	7.7	23.1	32.5	29.5	8.7	29.5	16.4	47.1
HMX	28.6	14.3	28.6	28.6	15.9	15.8	35.0	34.4	15.4	26.9
Nitroglycerin	25.0	15.0	15.0	45.0	10.1	17.1	16.4	54.6	17.9	25.0
Octanitroglycerin	0.0	25.0	25.0	50.0	15.3	19.5	21.9	41.9	18.4	0.2
RDX	28.6	14.3	28.6	28.6	10.2	15.1	37.7	37.0	22.2	23.8
PETN	27.6	17.2	13.8	41.4	16.5	21.3	14.1	46.2	12.7	26.1
TATP	54.5	27.3	0.0	18.2	51.2	28.1	1.3	18.6	3.7	53.9
TNT	23.8	33.3	14.3	28.6	22.5	33.5	11.3	31.4	4.3	17.7
Benzodiazepine	42.1	47.4	10.5	0.0	23.0	59.6	15.7	0.0	23.3	40.9
Perspex	53.3	33.3	0.0	13.3	52.6	34.3	1.4	13.4	1.8	52.4
Melamine	40.0	20.0	40.0	0.0	41.6	17.3	39.9	0.5	3.2	39.0
Polybutadiene	60.0	40.0	0.0	0.0	56.9	41.1	0.5	0.8	3.4	59.7
Nitric Acid	20.0	0.0	20.0	60.0	27.4	-1.5	12.6	61.6	10.7	15.9
Sucrose	48.9	26.7	0.0	24.4	49.0	26.2	0.8	24.2	1.0	49.2
PET	36.4	45.5	0.0	18.2	21.0	55.7	1.6	22.3	19.0	35.5
Polypropylene	66.7	33.3	0.0	0.0	72.3	29.4	1.6	3.3	7.8	67.2
Polyethylene	66.7	33.3	0.0	0.0	71.0	29.6	1.9	2.9	6.7	66.6
2-4-4-Trimethylpentane	75.0	25.0	0.0	0.0	75.0	21.1	1.0	3.6	5.4	76.4

Average error 12.50
Standard Deviation 9.54

Average error 2.47
Standard deviation 2.08

Figure 23: Predictions of the elemental compositions of the 10 explosives and 10 benign materials using the BGO and HPGe detectors. The error is defined as in section 4.4 and the ANN has been implemented in Keras.

7.5 Candidate Materials for Spectrally Selective Filters

Table 5: Table of elements that were analysed as potentially being suitable as spectrally selective filters. Their suitability was assessed using the total photon absorption cross sections at 2MeV, 4MeV and 6MeV [61].

Element	Atomic Number (Z)	Mass Density (gcm^{-3})	Molar Mass ($gmol^{-1}$)
Al	13	2.7	26.98
Si	14	2.329	28.085
P	15	2.69	30.97
S	16	2.07	32.06
K	19	0.862	39.1
Sc	21	2.985	44.96
Ti	22	4.506	47.87
Fe	26	7.87	55.85
Ni	28	8.908	58.693
Cu	29	8.96	63.546
Zn	30	7.14	65.38
Ga	31	5.91	69.72
Ge	32	5.323	72.63
As	33	5.727	74.92
Se	34	4.81	78.971
Sr	38	2.64	87.62
Nb	41	8.57	92.906
Ru	44	12.45	101.07
Ag	47	10.49	107.87
Cd	48	8.65	112.41
Sn	50	7.265	118.71
Ba	56	3.51	137.327
Nd	60	7.01	144.242
Er	68	9.066	167.259
W	74	19.25	183.84
Ir	77	22.56	192.22
Pt	78	21.45	195.08
Au	79	19.25	196.97
Tl	81	11.85	204.38
Pb	82	11.34	207.2
Bi	83	9.78	208.98